POLITECNICO DI TORINO
Repository ISTITUZIONALE

Thin-film-induced morphological instabilities over calcite surfaces

(Article begins on next page)

04 August 2020

Author for correspondence:

Riccardo Vesipa

e-mail: riccardo.vesipa@polito.it

Thin-film induced morphological instabilities over calcite surfaces

R. Vesipa[1] and C. Camporeale[1] and L. Ridolfi[1]

[1]Department of Environmental, Land and Infrastructure Engineering, Politecnico di Torino, Italy

Precipitation of calcium carbonate from water films generates fascinating calcite morphologies that have attracted the scientific interest over the last centuries. Nowadays, speleothems are no longer known only for their beauty but they are also recognized to be precious records of past climatic conditions, and research aims to unveil and understand the mechanisms responsible of their morphological evolution. In this paper we focus on crenulations, a widely observed ripple-like instability of the the calcite–water interface that develops orthogonally to the film flow. We expand a previous work providing new insights about the chemical and physical mechanisms that drive the formation of crenulations. In particular, we demonstrate the marginal role played by carbon dioxide transport in generating crenulation patterns, which are indeed induced by the hydrodynamic response of the free surface of the water film. Furthermore, we investigate the role of different environmental parameters, such as temperature, concentration of dissolved ions and wall slope. We also assess the convective/absolute nature of the crenulation instability. Finally, the possibility of using crenulation wavelength as a proxy of past flows is briefly discussed from a theoretical point of view.

1. Introduction

Water-driven morphological patterns are widespread in geological fluid mechanics, providing a plethora of examples, from glaciology [1–3] to river and sea morphodynamics [4,5] and karst environments [6,7]. One of the more remarkable case concerns the deposition of sinters from free surface flows and, in particular, the precipitation of calcite from dripping water [8,9].

Depending on many chemical and physical factors, the process of calcium carbonate deposition generates a wide variety of striking and sometimes weird morphologies, called speleothems. Remarkable examples are stalactites, stalagmites, draperies, helictites, and flowstones. The current efforts in studying and modelling the evolution of the karst environment is twofold. Firstly, it is interesting the understanding of the fundamental interactions between hydrodynamics and geochemistry, that are capable to shape mineral surfaces over a wide range of spatial scales (10^{-4}–10^4 m) [10]. Speleothems are some of the most spectacular and interesting natural beauties, and they are a clear example of the ability of a free surface flow to interact with chemical transport processes in order to carve a dissoluble substrate. Secondly, mineral deposition interacts with several industrial processes [11,12] and, more importantly, can be a precious proof of past climatic conditions. Measurable properties of the speleothems (e.g., mineral composition, calcite crystals type, etc...) can be related to the dripping water chemistry and to the surrounding environmental conditions in which the deposition occurred [13]. However, as pointed out by Fairchild *et al.* [14], speleothems records cannot yet be given a unique climatological meaning, and new methods for relating currently measurable properties with past conditions are constantly required.

The focus of this work are crenulations: ripple-like waves (see figure 1) that are widely observed over stalactites and flat vertical surfaces [7,8] and characterized by a wavelength ranging from centimetres to a tens of centimetres. Despite their pervasive occurrence, crenulations have received little scientific attention, and only recently two of us [7] have demonstrated that crenulations are the result of an interfacial morphological instability of the dynamical system composed by the calcite surface and the water falling film. The aim of this work is therefore twofold. Firstly, we extend the knowledge about the fundamental interactions between hydrodynamics and geochemistry by unveiling the physical and chemical mechanisms that induce the formation of crenulations. Secondly, we show that crenulations have a potential for being used as additional proxies for estimating the chemical composition and rate of past flows, thus playing an important role in paleo-climatic reconstructions.

The past studies that led to the current knowledge about the water driven morphological evolution of calcite surfaces focused on three fundamental issues: (i) the dependence of the macroscopic calcite precipitation rate on water chemistry, (ii) the role of the hydrodynamic conditions of the precipitating solution, and (iii) the mathematical modelling of speleothem shape evolution.

The first issue was addressed by using indirect methods: the monitoring of the changes in the solution chemistry during the calcite surface growth allowed the growth kinetics to be linked to chemical and physical parameters such as temperature, supersaturation state, and pH. There are three major categories of models for crystallization: surface complexation models, that take into account the reactions involving surface speciation [15]; summation of the elementary reaction theories, that describe growth rate as a function of multiple elementary reactions [16]; chemical affinity models developed in terms of free energy changes of precipitation reactions [17]. In particular, the precipitation model of Plummer [16] was successfully tested against laboratory experiments [18] and is now considered to be the most reliable model for assessing the precipitation and deposition rates of calcite (and thus the corresponding morphological modification of the mineral surface) [19]. For this reason, the Plummer model is incorporated in the present modelling approach.

The second issue (role of the falling film hydrodynamics) was studied by coupling calcite precipitation models with chemical diffusion profiles typical of several flow conditions, and allowed to understand how calcite precipitation occurs under static, laminar or turbulent films. [19,20]. More recently, numerical and experimental analysis are exploring the role of perturbations applied to laminar, free surface flow in developing instabilities that may ultimately lead to the formation of large scale morphologies [21].

The third issue (mathematical modelling of speleothems shape evolution) allowed the mechanisms underling the formation of several speleothems to be elucidated. Calcite terraces
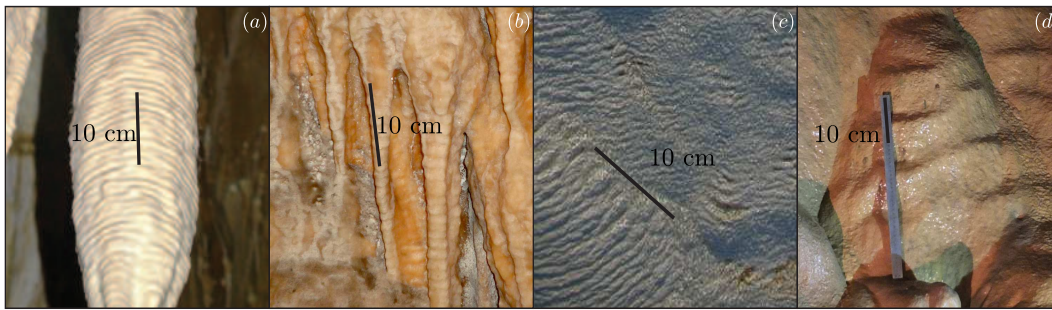
Figure 1. Crenulations in the Lehman caves, Nevada, USA (a) (http://www.nps.gov/grba); in the Jenolan Caves, NSW Australia (b) (http://www.flickriver.com/photos/nonlin/4760762574/); and in Pamukkale, Turkey (c) (personal source). Flow–stone that exhibits a dune-like instability in the Bossea caves, Italy (d) (personal source).

have been widely investigated over the last decades, both from a theoretical [22] and a numerical [21] point of view, and a robust understanding of the involved processes has been achieved. Stalactites and stalagmites have also attracted the interest of scientists, that have developed mathematical laws for the growth and the evolution of such speleothems [6,8,23]. At much lower spatial scales, researchers are also interested in unveiling the mechanisms involved in the formation and growth of dendrites in free surface flows [11]. The study of the interfacial stability of a calcite surface and a water film flowing on it has been addressed through an approximated depth-averaged hydrodynamic model only [24] (i.e., Dressler's equations), with no success in the prediction of crenulation formation.

In this work, we focus on the modelling of the interactions between: (i) a thin-film containing a solution of calcium carbonate and flowing over an inclined surface, whose dynamics are described by the Orr-Sommerfeld equations (i.e., the linearised version of the Navier-Stokes equations), written for free surface flows; and (ii) a surface of calcite whose morphological evolution is driven by the geochemistry of the calcium-carbonate-water ternary system. In a previous letter [7] it was demonstrated that crenulations are the result of a morphological instability of the film-surface interface. In this work we purse the following goals: (i) to describe a number of modelling and mathematical issues that in the preliminary letter were only briefly introduced. The explanation of the mathematical model and the techniques for its solution can be useful for the study of other karst morphologies. We also perform a minor algebraic correction to former results; (ii) to demonstrate the marginal role of carbon dioxide transport in the instability that leads to the formation of crenulations; (iii) to illustrate the chemo-physical mechanisms that induce the interface between the calcite surface and the water film to loose its stability, focusing in particular on the dynamics of the the free surface of the water film; (iv) to investigate the role of the different chemical and physical parameters on the crenulation dynamics and, in particular, how modifications of such parameters change the pattern wavelength; and (v) to study the convective and absolute nature of the crenulation instability.

2. Modelling aspects

The film-induced morphological evolution of a calcite surface is the result of the coupling between chemical and physical processes. The evolution of the wall morphology is in fact driven by the calcite deposition. The rate of calcite deposition is given by a number of different chemical reactions. The rate of such reactions depends on the reagent concentrations at the fluid-solid interface. Finally, such concentrations are influenced by the film flow field, which, in turn, is affected by the wall geometry. Therefore, a comprehensive mathematical description of such interactions requires to model: (i) the chemical reactions occurring at the fluid-solid interface (rate of precipitation of calcite), (ii) the film flow dynamics, (iii) the transport of chemicals in the fluid
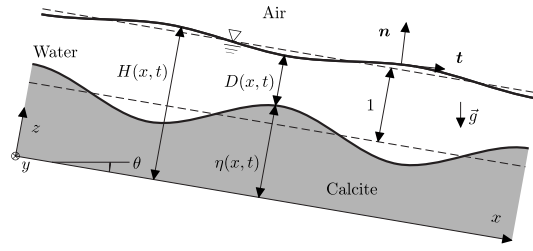
Figure 2. Sketch of the physical problem. The unperturbed flat bed and free surface (dashed lines) are also indicated.

film, and (iv) the morphological modifications induced by the deposition of calcite. In particular, we propose a mathematical model in which: (i) the rate of precipitation of calcite is evaluated by the celebrated Plummer-Wigley-Parkhurst (PWP) equation [16], (ii) the laminar Navier-Stokes equations are used for modelling the flow dynamics, (iii) the convection-diffusion equations describe the transport of chemicals in the fluid, and (iv) the morphological modifications induced by a calcite flow are evaluated with an Exner-Stefan like approach [5].

The model will allow us to pursue three fundamental goals. Firstly, we will demonstrate that crenulations are due to a morphological instability of the film-wall system. Previous studies gained important insights about the formation of large scale speleothems, but were unable to explain crenulations formations due to the approximations in the flow or chemical adopted models [24]. Secondly, we will describe the physical and chemical mechanisms that drive the formation of crenulations. Finally, we will show the marginal role of carbon dioxide transport in the formation of such karst morphologies.

Here after, model equations are written in dimensionless form. The longitudinal unperturbed fluid velocity at the free surface, $\tilde{u}_f$, and the mean flow depth, $\tilde{D}$, are used to scale lengths, velocities and times (tilde denotes dimensional quantities). In karst formations the Reynolds number is in the range $[10^{-4} - 10^{-1}]$. Under the assumption of a quasi-flat bottom, the flow is laminar [25], so that $\tilde{u}_f$ and $\tilde{D}$ can be derived from the Nusselt's flow solution

$$\tilde{u}_f = \left(\frac{g\nu R^2 \sin\theta}{2}\right)^{\frac{1}{3}}, \quad \tilde{D} = \left(\frac{2R\nu^2}{g\sin\theta}\right)^{\frac{1}{3}}, \tag{2.1}$$

where θ is the bed mean slope with respect to the horizon (see figure 2), $R = \tilde{u}_f\tilde{D}/\nu$ is the Reynolds number, ν is the fluid kinematic viscosity, and g is the gravity acceleration. A dimensionless right-handed Cartesian frame $\{x, z\}$ indicating the stream-wise and normal-to-the bed coordinates, respectively, is adopted. Notice that in order to address the fundamental dynamics of the crenulation instability, the cylindrical symmetry was assumed. The stream is bounded by the free surface $z = H(x, t)$ and by the water-calcite interface $z = \eta(x, t)$, where t denotes the time.

The concentration of calcium and bicarbonate will be scaled with the incoming calcium concentration $\mathcal{C} = [\text{Ca}^{2+}]_{x=0}$, where $[X_i]$ denotes dimensional concentration in mol·m^{-3} and subscript "i" refers to the i−th chemical species. Carbon dioxide concentration will be scaled with its equilibrium value at the free surface $\mathcal{H}p_c = [\text{CO}_2]_{z=H}$, where $\mathcal{H}$ is the Henry's law constant and p_c is the partial pressure. Accordingly, the chemical concentrations of the main species are $\{[\text{Ca}^{2+}], [\text{CO}_2], [\text{HCO}_3^-]\} = \mathcal{C}\{c_1, c_2\mathcal{H}p_c/\mathcal{C}, c_3\}$, where c_i are the corresponding dimensionless concentrations.

(a) Hydrodynamic model

Water film dynamics are described by the dimensionless Navier-Stokes and continuity equations for uncompressible flows

$$\mathbf{u}_{,t} + \mathbf{u} \cdot \nabla \mathbf{u} = -\nabla P + R^{-1} \nabla^2 \mathbf{u} + \mathbf{f}, \quad \nabla \cdot \mathbf{u} = 0, \qquad (2.2a,b)$$

where $\mathbf{u} = \{u, w\}$ is the velocity vector, the subscript comma denotes partial derivation in all equations, $\nabla = \{\partial/\partial x, \partial/\partial z\}$, P is the pressure, and $\mathbf{f} = 2/R\{1, -\cot\theta\}$ is the body force vector.
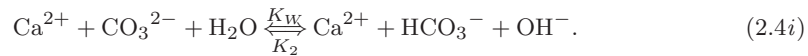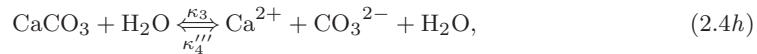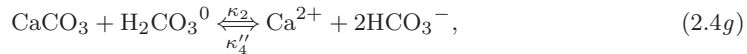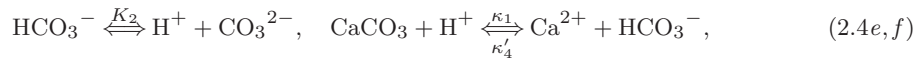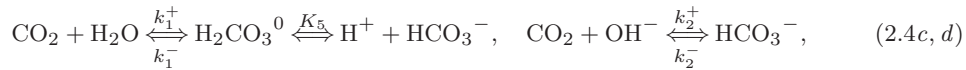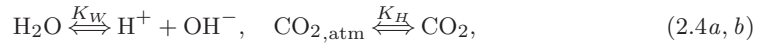
The boundary conditions of are [26]

$$H_{,t} + \mathbf{u} \cdot \mathbf{n}_H = 0, \quad \mathbf{n}_H \cdot \mathbf{T} \cdot \mathbf{t}_H = 0, \quad \mathbf{n}_H \cdot \mathbf{T} \cdot \mathbf{n}_H + \left[\frac{2}{R^5 \sin^2 \theta} \right]^{\frac{1}{3}} \frac{\mathcal{K}}{\mathrm{Ka}} = 0, \quad \text{at } z = \eta(x,t)$$

$$(2.3a,b,c)$$

$$\mathbf{u} \cdot \mathbf{n}_\eta = 0, \quad \mathbf{u} \cdot \mathbf{t}_\eta = 0, \quad \text{at } z = H(x,t), \qquad (2.3d,e)$$

where the unit vectors tangent and normal to the generic surface $\mathcal{S}$ read $\mathbf{t}_\mathcal{S} = \{1, \mathcal{S}_{,x}\}/(1 + \mathcal{S}_{,x}^2)^{1/2}$ and $\mathbf{n}_\mathcal{S} = \{-\mathcal{S}_{,x}, 1\}/(1 + \mathcal{S}_{,x}^2)^{1/2}$, respectively. Subscripts H and η refer to the free surface and the bottom, respectively, and $\mathcal{K} = H_{,xx}/(1 + H_{,x}^2)^{3/2}$ is the free surface curvature. The dimensionless Newtonian stress tensor is $\mathbf{T} = PR\mathbf{I} - 2\mathbf{D}$, where $\mathbf{I}$ and $\mathbf{D}$ are the identity matrix and the rate of strain tensor, respectively. Finally, the Kapitza number [27] reads $\mathrm{Ka} = l_c^2 g^{2/3} \nu^{-4/3}$, where l_c is the capillary length. Equations $(2.3a - c)$ state: (a) the kinematic condition, (b) the null shear stress, and (c) the occurrence of surface tension at the free surface $(z = H)$, while equations $(2.3d - e)$ state: (d) the impermeable surface, and (e) the non-slip fluid velocity at the bottom $(z = \eta)$.

(b) Chemical model

In an open-system with respect to CO_2, the chemical reactions responsible for the removal or deposition of calcite are [28,29]

$$H_2O \overset{K_W}{\Longleftrightarrow} H^+ + OH^-, \quad CO_{2,atm} \overset{K_H}{\Longleftrightarrow} CO_2, \qquad (2.4a,b)$$

$$CO_2 + H_2O \underset{k_1^-}{\overset{k_1^+}{\Longleftrightarrow}} H_2CO_3^0 \overset{K_5}{\Longleftrightarrow} H^+ + HCO_3^-, \quad CO_2 + OH^- \underset{k_2^-}{\overset{k_2^+}{\Longleftrightarrow}} HCO_3^-, \qquad (2.4c,d)$$

$$HCO_3^- \overset{K_2}{\Longleftrightarrow} H^+ + CO_3^{2-}, \quad CaCO_3 + H^+ \underset{\kappa_4'}{\overset{\kappa_1}{\Longleftrightarrow}} Ca^{2+} + HCO_3^-, \qquad (2.4e,f)$$

$$CaCO_3 + H_2CO_3^0 \underset{\kappa_4''}{\overset{\kappa_2}{\Longleftrightarrow}} Ca^{2+} + 2HCO_3^-, \qquad (2.4g)$$

$$CaCO_3 + H_2O \underset{\kappa_4'''}{\overset{\kappa_3}{\Longleftrightarrow}} Ca^{2+} + CO_3^{2-} + H_2O, \qquad (2.4h)$$

$$Ca^{2+} + CO_3^{2-} + H_2O \underset{K_2}{\overset{K_W}{\Longleftrightarrow}} Ca^{2+} + HCO_3^- + OH^-. \qquad (2.4i)$$

These reactions describe: (a) the dissociation of water into hydrogen- and hydroxyl-ions, (b) the physical dissolution of carbon dioxide in water, (c, d) the pH dependent conversion of carbon dioxide into hydrogen and bicarbonate, (e) the dissociation of bicarbonate into hydrogen- and carbonate-ions, and (f, g, h, i) the dissolution of calcite, also dependent on the solution pH. Notice that the total amount of available CO_2, namely $H_2CO_3^*$, is given by the sum of the carbonic acid $H_2CO_3^0$ and the dissolved carbon dioxide, i.e., $H_2CO_3^* = H_2CO_3^0 + CO_2$. All the equilibrium constants are listed in the Supplementary Material available online. The stoichiometry of the reactions listed above can be summarized as

$$CaCO_3 + CO_2 + H_2O \Longleftrightarrow Ca^{2+} + 2HCO_3^-. \qquad (2.5)$$
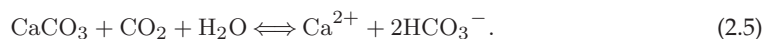
Therefore, for one Ca^{2+}-ion dissolved, one CO_2-molecule is taken from the solution and such molecule is replaced from the carbon dioxide in the atmosphere, as the system is open with respect

to CO_2 by the free surface. Notice that (2.5) holds true only for typical karst conditions. In fact, calcite dissolves at low pH, with the production of CO_2, and is precipitated at high pH, with the consumption of CO_2. Charge equilibrium is achieved if the concentrations of the different chemicals satisfy the following relation

$$2[\text{Ca}^{2+}] + [\text{H}^+] = [\text{HCO}_3{}^-] + 2[\text{CO}_3{}^{2-}] + [\text{OH}^-]. \tag{2.6}$$

In natural karst water $6 < \text{pH} < 8$; it follows that $[\text{OH}^-]$ and $[\text{CO}_3{}^{2-}]$ are very small compared to $[\text{Ca}^{2+}]$ and $[\text{HCO}_3{}^-]$, and they are usually neglected [19,28] allowing relation (2.6) to relax to

$$2[\text{Ca}^{2+}] = [\text{HCO}_3{}^-]. \tag{2.7}$$

In order to study the interactions between the water solution and the calcite surface, it is fundamental to refer to the ion activity rather than to ion concentration [16]. To this aim, we introduce the ionic strength of the solution as $I = \sum_i z_i^2 [X_i]/2$, where z_i is the ionic charge [19]. By considering the ternary system CaCO_3-H_2O-CO_2 and the relaxed electroneutrality condition, the ionic strength in natural karst water can be safely assumed as $I = 3[\text{Ca}^{2+}]$. The activity (measured in mol·m^{-3}) of the chemical species, $(X_i) = \gamma_i [X_i]$, is defined by the activity coefficient γ_i. For karst waters [29] in which $I < 10$ mol·m^{-3}, γ_i can be evaluated through the extended Debye-Hückel theory [30] as $\log \gamma_i = -Az_i^2 \sqrt{I}(1 + Bd_i\sqrt{I})^{-1} + e_i$ (coefficients are given in the Supplementary Material). Notice that activity coefficients are close to unity for $I < 10^{-3}$, and decrease to values between 0.6 and 0.9 for $I \sim 10^{-2}$, namely the ionic strength of a saturated solution of calcium carbonate in pure water at 298 K. [29].

At the calcite surface, the dissolution or deposition processes are characterized by the three fundamental reactions (2.4f-h) that macroscopically lead to a flux of calcium-ions. Several authors [19,31] found that a good quantification of both the dissolution and precipitation processes [32] is given by the Plummer-Wigley-Parkhurst (PWP) equation [16], which relates the calcium-ion flux with the local activities of several chemical species evaluated at the calcite-fluid interface. The PWP relation reads

$$\tilde{f} = -\kappa_1(\text{H}^+)_{z=\eta} - \kappa_2(\text{H}_2\text{CO}_3{}^0 + \text{CO}_2)_{z=\eta} - \kappa_3 + \kappa_4(\text{Ca}^{2+})_{z=\eta}(\text{HCO}_3{}^-)_{z=\eta}, \tag{2.8}$$

where $\tilde{f}$ is the deposition flux rate of calcium ions, subscript $z = \eta$ indicates that activities are evaluated at the calcite-fluid interface, κ_1 to κ_3 are the same rate constants reported in (2.4f-h), and κ_4 is a function of κ_4', κ_4'' and κ_4'''. To obtain a tractable version of (2.8), one has to relate the solution pH to the incoming calcium concentration $\mathcal{C}$ and the bicarbonate concentration to $[\text{Ca}^{2+}]$. After some algebra, one obtains

$$f = \rho_0 + \rho_1 c_1 \mid_{z=\eta} + \rho_2 c_2 \mid_{z=\eta} + \rho_3 c_1 \mid_{z=\eta}^2. \tag{2.9}$$

The mathematical derivation of (2.9) from (2.8), and the expression for the coefficients ρ_i are reported in the Supplementary Material. We stress that the approximation of relating the solution pH to the incoming calcium concentration $\mathcal{C}$ is necessary for obtaining a tractable version of (2.8) and, therefore, an analytical dispersion relation. The interpretation of the instability mechanism shown in section 4(c) will demonstrate the dominant role of the hydrodynamic processes in the crenulation formation. This allows to disregard some chemical details in the calcite deposition modelling.

Consider now the morphological alterations induced on the wall by a depositing calcite flux. The calcite flux modifies the bottom elevation according to the relation $\tilde{\eta}_{,\tilde{t}} = \varrho\tilde{f}$, where $\varrho \sim 10^{-4}$ m^3/mol is the molar volume of calcite. Such relation describes the dynamics of the wall, and plays the same role as the Exner and Stefan equations in other morphodynamic problems [2,5]. It must be noted that this macroscopic relation is valid only at dimensional scales larger than ~ 1 mm. Below this scale, the deposition of calcite cannot be longer considered uniform and does not lead to the formation of a smooth surface. Rather, the calcite surface consists of small, individual crystals protruding out [21]. Anyway, the fluid flows under laminar conditions. It follows that as

long as the amplitude of the roughness is much smaller the thickness of the film, then the small protuberances plays no significant role in determining the flow resistance [33].

By introducing the scaling $\tilde{f} = (\tilde{u}_f/\varrho)f$ we obtain the dimensionless equation that relates the bottom evolution to the calcite flow, namely

$$\eta_t - f = 0. \tag{2.10}$$

(c) Chemical transport model

The transport of the i-th chemical dissolved in the laminar water film is described by the convection-diffusion-reaction equation

$$c_{i,t} + \mathbf{u} \cdot \nabla c_i = P_i^{-1} \nabla^2 c_i + r_i, \tag{2.11}$$

and by the boundary conditions

$$c_{1,z}\big|_{z=H} = 0, \quad f = \chi \, c_{1,z}\big|_{z=\eta}, \quad c_2\big|_{z=H} = 1, \quad c_{2,z}\big|_{z=\eta} = 0, \tag{2.12a, b, c, d}$$

where c_i is the concentration (we recall that subscript 1 and 2 refer to calcium and carbon dioxide, respectively), $P_i = \tilde{D}\tilde{u}_f/\mathcal{D}_i$ is the Peclet number, $\mathcal{D}_i$ is the diffusion coefficient, r_i is a source or sink term, and $\chi = \varrho\mathcal{C}/P_1$ (notice that in our previous work [7], eq. 2.12b reported a wrong sign). If ion-pairing is neglected, calcium does not react with other species and the source-sink term r_1 is zero. At the free surface ($z = H$) no calcium is leaving or entering in the solution (no-flux, Eq. 2.12a). At the wall ($z = \eta$) the flux of calcium is directly proportional to the calcite flux (2.12b). In particular, when calcium is leaving (entering) the water film – i.e., deposition, $f > 0$ (dissolution, $f < 0$) – then the calcium concentration increases (decreases) from the water-calcite interface towards the free surface of the water film.

The dimensionless net production of carbon dioxide can be written as

$$r_2 = -k_1 c_2 + k_2(a_1 c_1 + a_2). \tag{2.13}$$

Refer to the Supplementary Material for the complete derivation of this last formula and for the expression of coefficients k_1 and k_2. At the bottom, $z = \eta$, the carbon dioxide flux is null, see Eq. (2.12d), while at $z = H$, the concentration of dissolved carbon dioxide is in equilibrium with the gas partial pressure in the atmosphere (2.12c). The assumption of carbon dioxide in Henry's law equilibrium at the free surface is commonly adopted [29], and is acceptable because if we set a fixed concentration of carbon dioxide at the top layer, then the CO_2 flux that exists from the water to the air is not hampered, as the gradient of the carbon dioxide concentration at the free surface is different from zero. This non zero flux corresponds to the carbon dioxide that leaves the water solution (degassing). We also stress that the carbon dioxide concentration at the top of the water film is in Henry's equilibrium with the carbon dioxide partial pressure that occurs close to the water film. This value can be different from the CO_2 concentration far from the free surface. Anyway, we will demonstrate (by a detailed sensitive analysis that spans orders of magnitude and reported in section 4.e) that crenulation formation is practically no sensitive to the external carbon dioxide partial pressure and, therefore, the assumptions introduced to model the carbon dioxide flux through the water air surface and its transport in air have a negligible effect on the global dynamics of the system.

3. Stability analysis

In the previous section, the mathematical model describing the film-induced spatio-temporal evolution of a calcite surface has been defined. It consists of: (i) the Navier-Stokes equations (2.2) for the modelling of the water film dynamics, flanked by the boundary conditions (2.3); (ii) the equation (2.9) – which quantifies the flux of calcite at the calcite-liquid interface as a function of the calcium-ions and carbon dioxide concentrations, evaluated at the calcite-liquid interface – and equation (2.10), which relates the temporal evolution of the bed with a given depositing calcite

flux; and (iii) the transport equations (2.11), with the boundary conditions (2.12$a - d$), that model the chemical transport in the water film.

In the following, the temporal derivatives of all equations, except in Eq. (2.10), are disregarded. This hypothesis (so-called quasi-steady approximation) is customary in many morphological problems [5]. It holds true when the morphological temporal evolution of the wall is much slower than the temporal dynamics of the fluid. The rigorous justification for this hypothesis is reported in the Supplementary Material.

In the real water-calcite karst system, one should also notice that the time-averaged calcite deposition rate is not constant along x. In fact, the deposition of calcite occurring while the film is flowing causes the average concentration of calcium to be progressively reduced from the initial concentrations at the source point. However, the film degassing and the loss of calcium occur on longitudinal scales (> 10 cm) much larger than the crenulation scale [7]. Therefore, in order to study the local stability of the water-calcite interface, these non-parallel effects can be disregarded [34].

Finally, we perform the transformation of variables $\zeta = [z - \eta(x,t)]/D(x,t)$. In this way the domain $[\eta, \eta + D = H]$ is mapped in the rectangular domain $[0, 1]$. This allows a correct setting of the boundary conditions at the free surface, that is a key point for the detection of the instability, as it will be shown in the following sections.

In order to study the stability of the flow-calcite interface to an infinitesimal perturbation, the dynamical system is forced with a harmonic disturbance of the bottom elevation

$$\eta = \eta_0(t) + \epsilon \hat{\eta} e^{i(\alpha x - \omega t)}, \tag{3.1}$$

where $\eta_0(t)$ is the uniform growth of the bottom elevation resulting from the uniform calcite deposition $\mathcal{F}$. The hat denotes the perturbed variable and α is the longitudinal wavenumber. The complex frequency reads $\omega = \omega_R + \omega_I$, where ($\omega_I$) and ($\omega_R/\alpha$) are the perturbation growth rate and celerity, respectively. Hereafter, subscript I (R) refers to the imaginary (real) part.

Equation (3.1) states that the deposition of calcite induces an upward translation of the bottom $\eta_0(t)$. Such translation acts over very long times, i.e., $d\eta_0(t)/dt \ll 1$. It follows that the alteration of the average bottom elevation does not induce any significant acceleration to the water film. From a mathematical point of view, the only effect of retaining $\eta_0(t)$ in (3.1) is to consider a rigid upward translation of the whole system. Therefore, $\eta_0(t)$ can be set to zero without any loss of generality.

The response of the governing equations to the bottom disturbance is then found by the following normal mode ansatz

$$\{u, w, p, c_1, c_2, f\} = \{\mathcal{U}(\zeta), 0, \mathcal{P}(\zeta), 1, \mathcal{C}_2(\zeta), \mathcal{F}\} + \epsilon\{\hat{u}, \hat{w}, \hat{p}, \hat{c_1}, \hat{c_2}, \hat{f}\}e^{i(\alpha x - \omega t)} + \text{c.c.} \tag{3.2}$$

where "c.c." denotes the complex conjugate, and $\mathcal{U}$, $\mathcal{P}$, $\mathcal{C}_2$ are the basic-state vertical-profiles of the longitudinal velocity, pressure and carbon dioxide concentration, respectively. As we focus on the very first stages of the morphology inception, perturbation amplitude is very small (i.e., $\epsilon \ll 1$), and the governing equations can be linearised around the basic state.

The unperturbed basic state can be found by collecting the terms $\mathcal{O}(\epsilon^0)$, and then solving the simplified problem. The PWP equation (2.9), then, becomes

$$\mathcal{F} = \rho_0 + \rho_1 + \rho_2 \mathcal{C}_2(0) + 2\rho_3 \tag{3.3}$$

where $\mathcal{C}_2(0)$ is the carbon dioxide concentration at the bottom. This equation states that, in unperturbed conditions, the flux of calcite $\mathcal{F}$ is uniform along x and over the time. In order to evaluate $\mathcal{C}_2(0)$ we have to consider the leading order terms of the carbon dioxide transport equation (Eq. [2.11], with $i = 2$) and its corresponding boundary conditions (2.12$c - d$), namely

$$\mathcal{C}_2''(\zeta) + k_1\mathcal{C}_2(\zeta) - a_1k_2 + a_2k_2 = 0, \quad \mathcal{C}_2(1) = 1, \quad \mathcal{C}_2'(0) = 0. \tag{3.4a, b, c}$$

By noticing that the parameter k_1 and k_2 are much smaller than 1, the solution of the previous equation can be approximated to

$$C_2(\zeta) = 1 + \frac{1}{2}(\mu - \mu\zeta^2), \tag{3.5}$$

that describes the parabolic profile of the carbon dioxide concentration, where $\mu = k_1 - k_2(a_1 + a2)$. We finally recall that from the horizontal $(x-)$ and vertical $(\zeta-)$ components of (2.2a) and the corresponding boundary conditions (2.3), the Nusselt's profiles for laminar flows $\mathcal{U}(\zeta) = 2\zeta - \zeta^2$ and $\mathcal{P}(\zeta) = 2(1 - \zeta)/\tan\theta$ are found.

Let's consider now the first order by collecting the terms $\mathcal{O}(\epsilon^1)$. The PWP equation (2.9), becomes

$$\hat{f} = (\rho_1 + 2\rho_3)\hat{c}_1(0) + \rho_2\hat{c}_2(0), \tag{3.6}$$

showing that the perturbation of the calcite flow $\hat{f}$ depends on the perturbations of the calcium $\hat{c}_1(0)$ and carbon dioxide $\hat{c}_2(0)$ concentrations at the water-wall interface.

In order to find $\hat{c}_1(0)$ and $\hat{c}_2(0)$, the first order of the boundary condition (2.11a) has to be considered. It reads

$$\hat{c}_i''(\zeta) + [\alpha_i + i\alpha P_i \mathcal{U}(\zeta)]\hat{c}_i(\zeta) + \hat{r}_i = 0, \tag{3.7}$$

where $\alpha_i = \{\alpha^2, \alpha^2 - k_1\}$.

Let us consider first the transport of calcium (i.e., $i = 1$). The linearised reactive term in the transport equation reads $\hat{r}_1 = 0$ and the linear form of the boundary conditions (2.12a, b) is $\hat{c}_1'(1) = 0$ and $\chi\hat{c}_1'(0) = \hat{d}\mathcal{F} + \hat{f}$. From a mathematical point of view, the origin of the term $\hat{d}\mathcal{F}$ is due to the adopted domain rectangularization, that transforms the derivatives in the right hand side of the latter boundary condition according to $d/dz \to 1/D(x,t)d/d\zeta$. Implementation of this boundary condition is a fundamental step, but critical, as it involves also the unknown calcite flux perturbation $\hat{f}$. This difficulty is by-passed by defining the function $\mathcal{I}(\zeta)$ such that $\hat{c}_1(\zeta) = (\hat{d}\mathcal{F} + \hat{f})\mathcal{I}(\zeta)/\chi$. In this way, equation (3.7) and its boundary conditions become

$$\mathcal{I}''(\zeta) + [\alpha^2 + i\alpha P_1 \mathcal{U}(\zeta)]\mathcal{I}(\zeta) = 0, \quad \mathcal{I}'(0) = 1, \quad \mathcal{I}'(1) = 0, \tag{3.8a, b, c}$$

from which $\mathcal{I}(\zeta)$ can be evaluated. Finally, the vertical profile of the calcium concentration perturbation can be evaluated as

$$\hat{c}_1(\zeta) = \mathcal{I}(\zeta) \cdot (\hat{d}\mathcal{F} + \hat{f})/\chi. \tag{3.9}$$

Let us consider now carbon dioxide (i.e., $i = 2$). The reactive term of the transport equation (2.13a) is linearised to $\hat{r}_2$. The term $\hat{r}_2$ contains the unknown calcite flux perturbation $\hat{f}$, a feature that complicates the solution of (3.7). To this aim, $\hat{r}_2$ is written as the sum of two contributions, namely, $\hat{r}_2 = \hat{r}_{\mathcal{L}} + \hat{f}\hat{r}_{\mathcal{M}}$, being $\hat{r}_{\mathcal{M}} = \chi^{-1}a_1 k_2 \mathcal{I}(\zeta)$, and

$$\frac{\hat{r}_{\mathcal{L}}}{\beta} = \hat{d}(2 - k_1) + \alpha^2\zeta + [(1 - \hat{d})2iP_2 + \hat{d}(k_1 - \alpha^2)]\zeta^2 + 2i(\hat{d} - 1)P_2\zeta^3 + \hat{r}_{\mathcal{M}}\mathcal{F}\hat{d}, \tag{3.10}$$

It follows that $\hat{c}_2$ has the same structure of $\hat{r}_2$, namely $\hat{c}_2(\zeta) = \mathcal{L}(\zeta) + \hat{f}\mathcal{M}(\zeta)$. In this way equation (3.7) can be recast as the independent boundary value differential problems

$$\mathcal{L}''(\zeta) + [\alpha^2 - k_1 + i\alpha P_2 \mathcal{U}(\zeta)]\mathcal{L}(\zeta) - \hat{r}_{\mathcal{L}} = 0, \quad \mathcal{L}(1) = 0, \quad \mathcal{L}'(0) = 0, \tag{3.11a − c}$$

$$\mathcal{M}''(\zeta) + [\alpha^2 - k_1 + i\alpha P_2 \mathcal{U}(\zeta)]\mathcal{M}(\zeta) - \hat{r}_{\mathcal{M}} = 0 \quad \mathcal{M}(1) = 0, \quad \mathcal{M}'(0) = 0. \tag{3.12a − c}$$

The vertical profile of the carbon dioxide perturbation is finally given

$$\hat{c}_2(\zeta) = \mathcal{L}(\zeta) + \hat{f}\mathcal{M}(\zeta). \tag{3.13}$$

We now consider the first order approximation of (2.10), namely

$$\hat{f} = \omega, \tag{3.14}$$

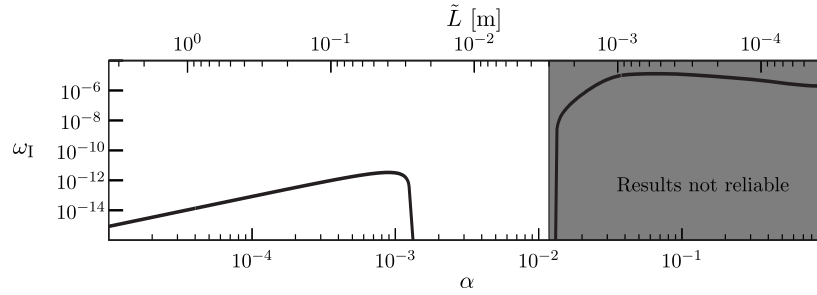that equals the perturbation complex frequency with the perturbation of the calcite flow.

Figure 3. Growth rate as a function of the wavenumber α (bottom axis) and $\tilde{L}$ (upper axis) for benchmark conditions $\mathbf{l}_B$ and $R = 10^{-3}$. The grey zone denotes the wavenumbers for which the model is not able to provide reliable results ($\tilde{L} < 2$ mm).

Finally, we substitute (3.9), (3.13) and (3.14) in the equation (3.6), obtaining the dispersion relation

$$D(\omega, \alpha) = \omega - \frac{\mathcal{F}\hat{d}(\rho_1 + 2\rho_3)\mathcal{I}(0) - \rho_2\chi\mathcal{L}(0)}{\chi[\rho_2\mathcal{M}(0) - 1] - \mathcal{I}(0)(\rho_1 + 2\rho_3)} = 0. \tag{3.15}$$

The dispersion relation $D(\omega, \alpha)$ relates the growth rate (ω_I) and the celerity (ω_R/α) of the crenulations forming on the water-calcite interface to the wavenumber α. By just observing the dispersion relation, one recognizes that crenulation dynamics are influenced by: (i) the water chemistry, through the term $\mathcal{F}$, as evaluated through (3.3); (ii) the perturbation of water depth, $\hat{d}$, that can be obtained by the solution of the linearised Navier Stokes equations (2.2$a - b$) and depends on the wavenumber to a great extent (the complete procedure for the evaluation of $\hat{d}$ is reported in the Supplementary Material); and (iii) the perturbation of concentrations of chemical at the interface through the terms $\mathcal{I}(0)$, $\mathcal{L}(0)$ and $\mathcal{M}(0)$. The mathematical procedures adopted for solving $\hat{d}$, $\mathcal{I}(0)$, $\mathcal{L}(0)$ and $\mathcal{M}(0)$ by the semi-analytic Frobenius method are reported in the Supplementary Material.

4. Results

(a) Morphological instability of the water-calcite interface

For a given set of parameters, the linear dynamics of the fluid-calcite interface in the wavenumber space can be summarized by three scalar quantities. The first one is the maximum growth rate of the perturbation, namely $\omega_{I,\max} = \max\{\text{Im}[\omega(\alpha)]\}$. For $\omega_{I,\max} > 0$ ($\omega_{I,\max} < 0$) the solid-calcite interface is unstable (stable) and the crenulation pattern will (will not) shape the calcite surface. The second key quantity is the most unstable wavenumber $\alpha_{\max}$, i.e., the wavenumber that maximizes the growth rate of the perturbation (i.e., $\omega_I[\alpha_{\max}] = \omega_{I,\max}$). According to the linear theory, $\alpha_{\max}$ is the wavenumber that is selected during the evolution of infinitesimal crenulations. The last quantity is the phase velocity of the most amplified wavenumber, i.e., the migration velocity of the crenulation ridges. It reads $v_{p,\max} = -\text{Re}[\omega(\alpha_{\max})]/\alpha_{\max}$ and for $v_{p,\max} > 0$ ($v_{p,\max} < 0$) the crenulation pattern will migrate downstream (upstream).

In figure 3, the growth rate is plotted as a function of the wavenumber for $R = 10^{-3}$ and for a fixed set of benchmark parameters, well representative of the karst environment. We consider the typical conditions $\mathbf{l}_B = \{\theta_B, T_B, p_{c,B}, \mathcal{C}_B\} = \{\pi/2, 282 \text{ K}, 350 \text{ ppm}, 350 \text{ ppm}\}$, where $\mathbf{l}$ is the vector of control parameters and subscript "B" denotes benchmark conditions. By setting $\theta_B = \pi/2$ we firstly focus our analysis on vertical surfaces (e.g., stalactites) where crenulations are very likely to be observed.

The curve $\omega_I(\alpha)$ exhibits two maxima, the first one at $\alpha \simeq 10^{-3}$ and a second one at $\alpha \simeq 10^{-1}$. Recalling that the dimensional wavelength and the dimensionless wavenumber are related through $\tilde{L} = 2\tilde{D}\pi/\alpha$, the first maximum selects a pattern with wavelength of the order of 30
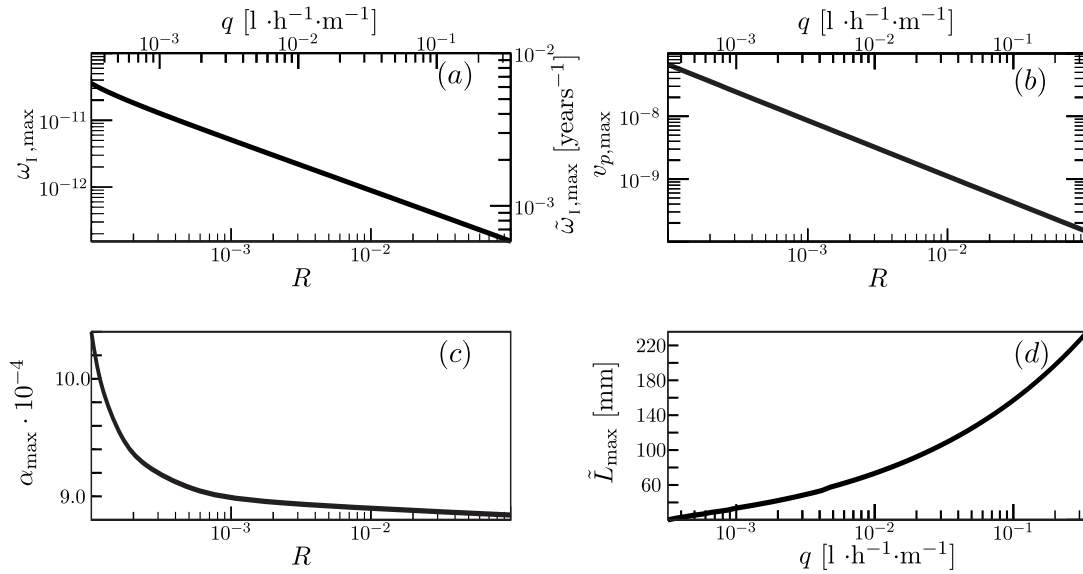
Figure 4. The maximum attained growth rate (a), the phase velocity of the most unstable wave (b), the most amplified wavenumber (c) and the dimensional most amplified wavelength (d) are shown as a function of the film Reynolds number, R, or of the film unitary flow rate, q. Benchmark conditions l_B are considered.

mm, which is the typical crenulation wavelength observed in the karst environment ($\sim 10^{-2}$ m). Instead, the second maximum selects a pattern with a wavelength of the order of 0.5 mm, which is the typical size of calcite dendrites (several tens of microns [35]). Such second maximum falls in a zone where the validity of the proposed model is questionable, and it is here reported only for completeness. It can be observed, in fact, that the unstable zone on the right arises for wavelength smaller than ~ 2 mm. As anticipated in section 2(b), at such longitudinal scales the deposition of calcite cannot be considered uniform. In fact, the sinter surface consists of a multitude of small individual crystals protruding out. Therefore, for $\alpha > 10^{-2}$ ($\tilde{L} < \sim 1$ mm) one of the main assumption of the model (i.e., Eq. 2.10) is no longer valid, and thus the model results are not reliable. A more sophisticated theory would be required to model the very complex crystal and dendrite formation. In particular, the description of the calcite precipitation kinetics as well as the morphological modifications induced by the sinter deposits should be further improved. However, these dendrite scales are out of the scope of this study; therefore, we limit the analysis of $\omega_{I,max}$, α_{max} and $v_{p,max}$ to $\alpha < 10^{-2}$, and we will not consider unstable zones occurring for $\alpha > 10^{-2}$ to be physically relevant for crenulation dynamics.

In figure 4 the dependence of the crenulation dynamics on the Reynolds number is illustrated. Reynolds number varies from 10^{-4} up to 10^{-1}, a range that comprises most of the flow conditions found in the karst environment. It can be observed (panel a) that the maximum growth rate is always positive (the calcite-flow interface is always unstable to crenulations) and it decreases when the flow rate (i.e., R) increases. In figure 4b the dynamics of the crenulation phase velocity can be observed. In vertical surfaces, crenulations always migrate downstream ($v_{p,max}$ is always positive), and the migration velocity strongly decreases for increasing R. Figure 4c demonstrates the very small influence of R in defining the most amplified wavenumber: while R spans three orders of magnitude ($R \in [10^{-4}, 10^{-1}]$), α_{max} remains in the very narrow range $[9.0, 10.40] \cdot 10^{-4}$. Dimensionally, instead, while the unitary flow q spans in the range $[10^{-4}, 10^{-1}]$ l·h^{-1}·m^{-1} the pattern wavelength (i.e., the most amplified wavelength $\tilde{L}_{max} = 2\tilde{D}\pi/\alpha_{max}$) is in the range $[20 - 220]$ mm (figure 4d).

These results confirm the ability of the model to capture the typical wavelengths observed in karst environment. For $R \sim 10^{-3}$, it predicts the occurrence of centimetric waves, namely

Table 1. Numerical value of the terms of (3.15), evaluated for benchmark condition adopted in the previous section $\mathbf{l}_B$, $R = 10^{-3}$ and $\alpha = 0.95 \cdot 10^{-3}$ (the most unstable wavenumber that arises for these parameters). We recall that $\chi = 1.8 \cdot 10^{-4}$.

$\mathcal{F}$	ρ_1	ρ_2	ρ_3
$1.7 \cdot 10^{-5}$	$5.6 \cdot 10^{-10}$	$5.1 \cdot 10^{-8}$	$1.7 \cdot 10^{-5}$
$\hat{d}$	$\mathcal{I}(0)$	$\mathcal{L}(0)$	$\mathcal{M}(0)$
$-5 \cdot 10^{-7} + 5\mathrm{i} \cdot 10^{-5}$	$-1.2 + 8.4\mathrm{i} \cdot 10^2$	$1.7 \cdot 10^{-6} - 1.2\mathrm{i} \cdot 10^{-8}$	$1.3 - 2.1\mathrm{i} \cdot 10^3$
$\mathcal{F}\hat{d}(\rho_1 + 2\rho_3)\mathcal{I}(0)$	$\rho_2\chi\mathcal{L}(0)$	$\chi[\rho_2\mathcal{M}(0) - 1]$	$\mathcal{I}(0)(\rho_1 + 2\rho_3)$
$(2.4 + 0.028\mathrm{i}) \cdot 10^{-11}$	$(-1.6 + 0.011\mathrm{i}) \cdot 10^{-17}$	$(-1.8 + 0.00019\mathrm{i}) \cdot 10^{-4}$	$(-0.0041 + 2.9\mathrm{i}) \cdot 10^{-2}$

crenulations, characterized by downstream migration (in vertical surfaces) and a relatively fast growth rate. For $R \sim 10^{-1}$, the model predicts the formation of longer waves ($\sim 10^{-1}$ m) that migrate downstream, and with a growth rate much lower than crenulations. Also these dune-like long waves (see figure 1d) are common morphologies on flowstones (i.e., the inclined side walls of the caves).

(b) The marginal role of carbon dioxide transport

We now explore the role played by the chemical and physical phenomena responsible of the morphological instability of the water-calcite interface and of the selection of the most unstable wavelength. To this aim, we numerically quantify the different terms appearing in the dispersion relation (3.15).

Let us firstly compare the numerical value of coefficients ρ_1, ρ_2 and ρ_3, that link the rate of calcite deposition to the bottom concentrations c_1 and c_2 by the PWP equation (2.9). By considering the typical numerical values of these coefficients (see Table 1), it can be observed that the term $(\rho_1 + 2\rho_3) \simeq 10^{-5}$ exceeds of three orders of magnitude the term $\rho_2 \simeq 10^{-8}$. We now compare the magnitudes of terms $\mathcal{I}(0)$, $\mathcal{L}(0)$ and $\mathcal{M}(0)$ introduced to evaluate the perturbation of carbon dioxide and calcium concentration at the bottom, namely $\hat{c}_2(0)$ and $\hat{c}_1(0)$ (see section 3). Table 1 shows that $\mathcal{I}(0)$ and $\mathcal{M}(0)$ are of the same order of magnitude, while $\mathcal{L}(0)$ is significantly lower.

We have now the elements to detect the dominant terms of the dispersion relation (3.15). Let us firstly consider the numerator. The real and the imaginary part of $\mathcal{F}\hat{d}(\rho_1 + 2\rho_3)\mathcal{I}(0)$ are six orders of magnitude bigger than $\rho_2\chi\mathcal{L}(0)$. This last term can be therefore disregarded. Consider now the denominator of (3.15) and, in particular, the term $\chi[\rho_2\mathcal{M}(0) - 1]$ where $\rho_2\mathcal{M}(0) \sim 10^{-11}$ can be disregarded: the real part of $\chi[\rho_2\mathcal{M}(0) - 1]$ equals $-\chi$ while its imaginary part is 10^6 times smaller than the imaginary part of the other term $\mathcal{I}(0)(\rho_1 + 2\rho_3)$, and thus it is negligible.

Summing up, the terms related to the carbon dioxide transport $\mathcal{L}(0)$ and $\mathcal{M}(0)$ are comparable to the term related to calcium transport $\mathcal{I}(0)$, but the formers are heavily penalized by the coefficients ρ_2 that is very small, and the dispersion relation can be approximated as

$$\omega = \frac{\rho_1 + 2\rho_3}{\chi}(\hat{f} + \mathcal{F}\hat{d})\mathcal{I}(0) = (\rho_1 + 2\rho_3)\hat{c}_1(0) = (\rho_1 + 2\rho_3)[c_{\hat{f}}(0) + c_{\hat{d}}(0)], \qquad (4.1)$$

that states: (i) crenulation dynamics are driven by the response of the calcium concentration to the bed perturbation, and (ii) the transport of carbon dioxide does not play any significant role. In particular, crenulation growth rate (ω_I) and celerity (ω_R/α) are proportional, through the coefficient ($\rho_1 + 2\rho_3$), to the perturbation of calcium concentration at $\zeta = 0$, $\hat{c}_1(0)$. This latter term is made up of two components: (i) $c_{\hat{f}}(0) = \hat{f}\mathcal{I}(0)/\chi$, that describes the effect of the calcite depositing flow on the calcium concentration, and (ii) $c_{\hat{d}}(0) = \mathcal{F}\hat{d}\mathcal{I}(0)/\chi$ that describes the effect of the water depth on the calcium concentration.
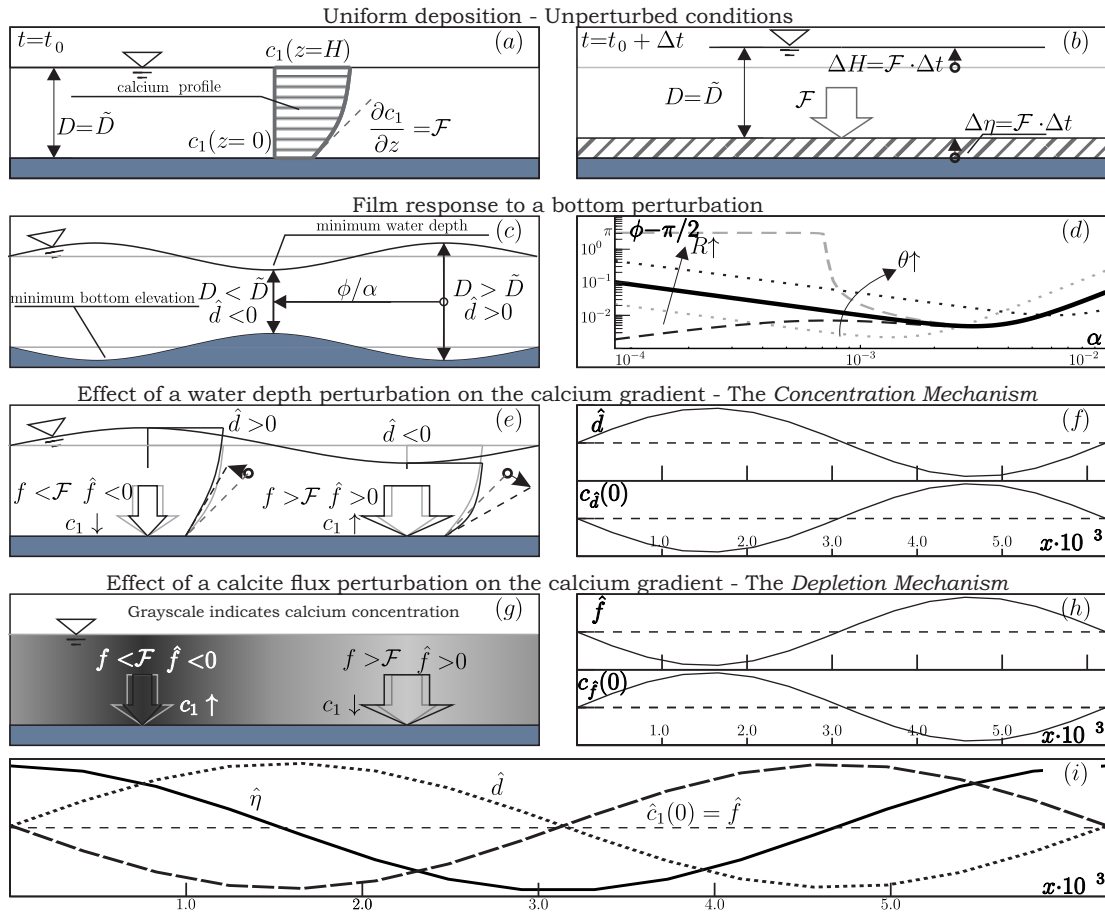
Figure 5. (a, b) Uniform deposition in the time interval Δt: the bed elevation increases of $\Delta \eta$ and the film translates accordingly. (c) Example of a phase lag $\phi = \pi$ between the bottom and the water depth. (d) Phase lag excess with respect to $\pi/2$ (i.e., $\phi - \pi/2$) vs. wavenumber α evaluated for $\theta = \pi/2$, $T = 282$ K and $R = 10^{-3}$ (full line); $R = 10^{-4}$ (dashed); and $R = 10^{-2}$ (dotted); Grey dotted and dashed lines refer to $\theta = 0.95\pi/2$ and $\theta = 1.05\pi/2$, respectively, and $(R = 10^{-3}$, $T = 282$ K). (e) Conceptual scheme of the dilution mechanism (the unperturbed calcium profile is reported in grey). (f) Behaviour of $\hat{d}$ along one wavelength and the corresponding response of the calcium concentration $c_{\hat{d}}(0)$. (g) Conceptual scheme of the diffusion mechanism (the greyscale indicates calcium concentration). (h) Behaviour of $\hat{f}$ along one wavelength and the corresponding response of the calcium concentration $c_{\hat{f}}(0)$. (i) Overall spatial behaviour of the perturbations along one wavelength. Panels (f, h, i) refer to $\{R, \theta, T, p_c, \mathcal{C}, \} = \{ 10^{-3}, 1.1\pi/2, 282$ K,1000 ppm,190 ppm $\}$ and $\alpha = 1.01 \cdot 10^{-3}$ (the most unstable wavenumber).

We finally recall that after using (3.14), equation (4.1) can be rearranged in the final form

$$\omega = \frac{\mathcal{F}\hat{d}}{1 - A\mathcal{I}(0)}, \tag{4.2}$$

with $A = (\rho_1 + 2\rho_3)/\chi$, showing that the growth rate is proportional to the film depth perturbation $\hat{d}$.

(c) The key mechanisms driving crenulation formation

Relation (4.1) shows that the formation of crenulations can be understood by investigating how the film depth perturbation, $\hat{d}$, and the perturbation of the calcite flow, $\hat{f}$, alter the calcium

concentration at the wall. For the sake of clarity, we do not consider the effect of the chemical advection, that complicates the picture without any gain in the understanding of the main dynamics. To this aim, the term $i\alpha P_1 \mathcal{U}(\zeta)$ can be discarded in (3.8a).

Preliminary, we have to elucidate how the free surface and, in turn, the water depth respond to a bottom perturbation. We therefore focus on the phase angle, ϕ, between the flow depth perturbation induced by a bottom topography and the topography itself. Such angle is linked to the location of the minimum flow depth ($\min[\hat{d}]$, figure 5c) and three cases can occur: (i) the most severe shallowing occurs over the downstream side of a bump (i.e., where $\hat{\eta} > 0$ and $\partial \hat{\eta}/\partial x < 0$). In this case the phase angle between $\hat{d}$ and $\hat{\eta}$ is in the range $]\pi/2, \pi[$; (ii) $\min[\hat{d}]$ takes place over the upstream side of a bump ($\hat{\eta} > 0$ and $\partial \hat{\eta}/\partial x > 0$) and ϕ falls in the range $]\pi, 3\pi/2[$; and (iii) $\min[\hat{d}]$ occurs over a depression (i.e., $\hat{\eta} \leq 0$) and the phase angle results in the range $[0, \pi/2]$ or $[3\pi/2, 2\pi]$, depending on the sign of $\partial \hat{\eta}/\partial x$. It can be observed (black bold line in panel 5d) that for the typical values $R = 10^{-3}$ and $\theta = \pi/2$ occurring in karst systems, the phase angle between $\hat{d}$ and $\hat{\eta}$ is slight larger than $\pi/2$, for all the wavenumber considered. Therefore, the most severe film thinning always occurs over the downstream side of the bumps. The black dotted (black dashed) line in figure 5d shows that a reduction (increase) of the Reynolds number induces only a small downward (upward) translation of the phase-wavenumber curves. Also a reduction of the wall slope (dotted gray line) does not affect significantly the behaviour. Instead, in the case of overhanging walls, it can be observed (dashed gray line) that for low wavenumbers, the phase angle switches from values slightly greater than $\pi/2$ to values slightly smaller than $3\pi/2$. Physically, the most severe film shallowing occurs on the upstream side of the protrusions. The switching of the position of $\min[\hat{d}]$ from the downstream to the upstream side of the bumps when θ exceeds $\pi/2$ causes several changes in the macroscopic behaviour of the crenulations pattern (e.g., the switch of the migration direction) that will be described in the following sections.

We now investigate how the calcium concentration at the film bottom is altered by a water depth perturbation, $\hat{d}$. Panel 5f reports the spatial behaviour over one wavelength of the perturbed water depth $\hat{d}$ and the corresponding perturbation induced in the calcium concentration at the wall, namely $c_{\hat{d}}(0)$: it can be observed that at the location where the water depth is minimum, the calcium concentration is maximum. Let us investigate the physics behind this behaviour. When the film depth reduces (see the right part of panel e), the corresponding calcium profile (black line) becomes more steep with respect to the unperturbed profile (gray line, see also panel a). The consequence of a steeper calcium profile (see dashed black and gray lines in panel 5e) is that more calcium ions are pumped through diffusion from the film towards the wall. This high flux of calcium ions, in turn, rises the calcium concentration at the wall. It follows that the calcite flow rate results increased (see linearised PWP equation 3.6) and also the bottom elevation growth rate increases (see the bottom evolution equation 2.9). The opposite happens if an increase of the water depth occurs ($\hat{d} > 0$, shown in the left part of panel e): the calcium profile becomes less steep than the unperturbed calcium profile and the concentration $c_{\hat{d}}(0)$ at the bottom decreases. Accordingly, the calcite flow rate $\hat{f}$ and the bottom elevation growth rate $\hat{\eta}_{,t}$ diminish.

At the beginning of this section we have shown that the minimum water depth always occurs over a bump ($\hat{\eta} > 0$). We have then demonstrated that the highest increment of calcite deposition ($\max[\hat{f}]$) occurs at the location in which $\min[\hat{d}]$ takes place. It follows that $\max[\hat{f}]$ occurs in zones where $\hat{\eta}$ is already larger than zero, while $\min[\hat{f}]$ takes place in zones where $\hat{\eta} < 0$. Physically, the deposition of calcite is promoted over protrusions and inhibited over depressions. This mechanism accelerates the deposition over bumps and slows the precipitation over depressions. Therefore, the unevenness of the surfaces is increased and a crenulation pattern emerges. This process that induces the morphological instability of the system will be hereafter referred as *concentration mechanism*, in order to underline the concentration of calcium at the bottom induced by the film thinning. We recall that hydrodynamically induced alterations of the chemical gradients were demonstrated to play a key role in the generation of other calcite morphologies [21].
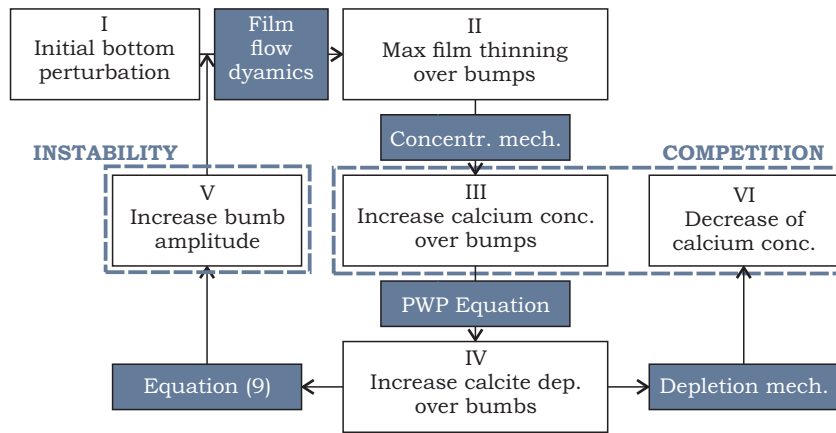
Figure 6. Conceptual scheme describing the morphological evolution of a calcite wall.

Consider now the feedback of the calcite flux on the calcium concentration. In panel (h) the spatial behaviour over one wavelength of the calcite flux, $\hat{f}$, and the perturbation induced in the calcium concentration at the wall, $c_{\hat{f}}(0)$, are shown: it can be observed that when the calcite flux reaches its maximum, the calcium concentration is minimum. Namely, a higher rate of calcite precipitation induces a higher rate of consumption (and thus removal) of calcium in all the film depth (panel g) and, in particular, near the wall. According to equations (3.6) and (2.9), also the calcite flow rate and the bottom elevation growth rate are reduced. The opposite happens if a lower rate of calcite deposition occurs ($\hat{f} < 0$, on the left in the panel g): the calcium concentration increases and, in turn, also the calcite flow rate $\hat{f}$ increases. This process alone, that in the following will be referred as *depletion mechanism*, plays a stabilizing role. In fact, at the locations in which an excess of calcite precipitation occurs, a reduction of the calcium concentration is induced. Such reduction of calcium concentration, in turn, halts the calcite deposition excess.

Examine now the full response of the system to perturbations $\hat{d}$ and $\hat{f}$, with the help of figures 5i and 6. The film responds to an initial bottom perturbation (I) with a film depth perturbation (II). Recall (panel 5d and 5i) that the maximum film thinning (i.e., min[$\hat{d}$]) occurs over protrusions ($\hat{\eta} > 0$). As a consequence of the concentration mechanism, an increase of calcium concentration occurs where the film shallows (III). According to the PWP equation, at the locations in which an increment of calcium concentration occurs, also an increment of the calcite flow takes place (IV). The effect of this increment of the calcite flux is twofold. On one side, it induces an increment of the bottom elevation and, since the highest calcite deposition flux, max[$\hat{f}$], takes place over wall protrusions ($\hat{\eta} > 0$), these protuberances grow. The growth of bumps amplitude (V) induces, in turn, the increment of the amplitude of all the other perturbations, giving rise to a positive feedback and to the instability that generates the pattern of crenulations. On the other side, the increment of calcite deposition induces (by means of the depletion mechanism) a reduction of the calcium concentration (VI). This depletion-induced reduction of calcium is in competition with the increment of calcium driven by the concentration mechanism. We stress that the depletion mechanism is a stabilizing feedback process that damps the calcite flow perturbations induced by the concentration mechanism.

The same mechanisms are also found if the convection of chemicals is restored. In such case, we observe only a slight downstream phase lag between the water depth perturbation and the calcite perturbed flow. Anyway, the key processes inducing the instability – concentration mechanism and competition with the depletion mechanisms – remain the same.
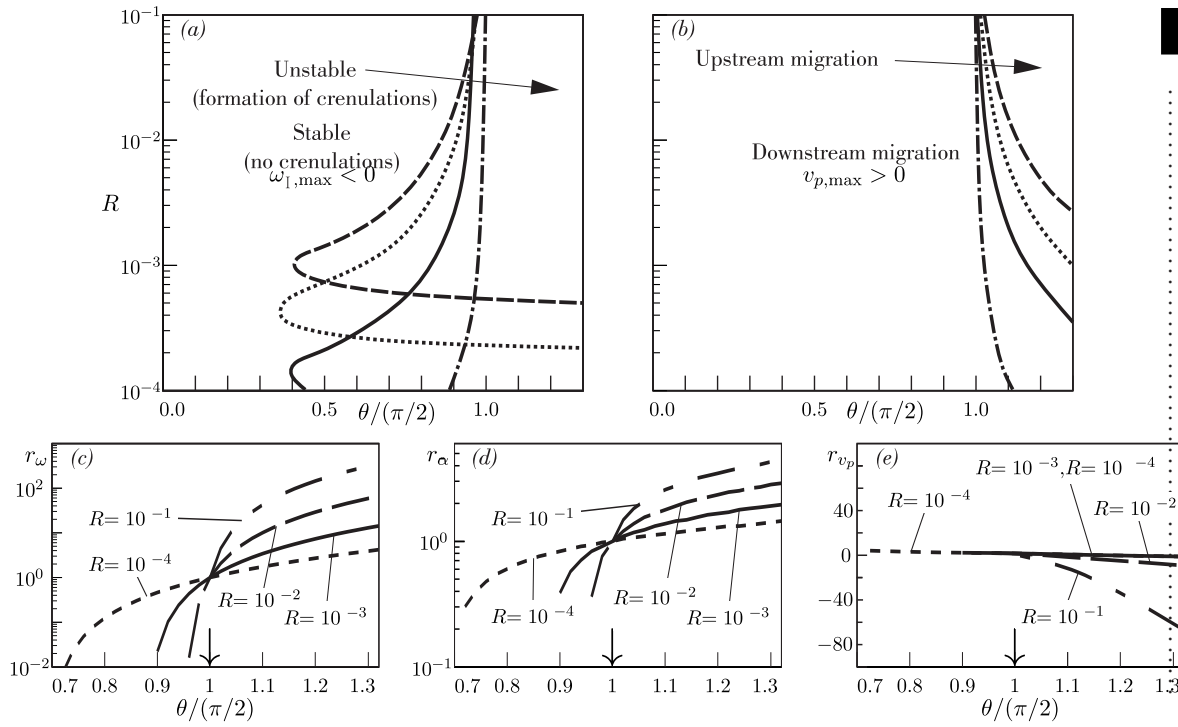
Figure 7. (a) Marginal stability curves. (b) Upstream-downstream migration regions (lines correspond to $v_{p,\max}$=0). Benchmark conditions (solid) but: $\mathcal{C}$=1000 ppm (dotted), T=303K (dashed), p_c=10000 (dot-dash) ppm. In the lower row, the dependence of r_ω, r_α and r_{v_p} on θ is shown. The vertical arrow marks $\theta = \pi/2$.

(d) The key role of the wall slope

In the previous section, we have demonstrated the crucial role of the film fluid dynamics in determining the stability of the calcite-flow interface. It follows that, being the flow characteristics (in particular the response of the film depth to a bottom perturbation) influenced to a great extent by the Reynolds number and by the wall average slope, these quantities impact the dynamics of crenulations. In figure 7a, the marginal stability curves (i.e., points where the growth rate $\omega_{\mathrm{I},\max}$ is null) are reported in the $\theta - R$ plane. It can be observed that for relatively high Reynolds numbers $(R > 10^{-2})$ crenulation formation is only possible on walls almost vertical, or steeper ($\theta > 0.9\pi/2$) while for progressively lower values of R the instability occurs even for significantly lower slope, so that crenulations can appear when the wall average slope is as low as $\pi/4$. With a further reduction of R the system becomes stable to crenulations and, for a given θ, the marginal stability curves exhibit a threshold value R_c that separates the zone of stability ($R < R_c$) from the zone of instability ($R > R_c$). Notice that the critical Reynolds number, R_c, above which crenulations form is highly dependent on temperature and water chemistry, as shown by the different lines of panels 7$a - b$, evaluated by changing some parameters from the benchmark condition.

In figure 7b the locus of the points that have a null phase velocity, namely $v_{p,\max} = 0$, is reported. Depending on the parameters, crenulations can therefore migrate either downstream $(v_{p,\max} > 0)$ or upstream $(v_{p,\max} < 0)$. In particular, this latter case is only observed for overhanging walls ($\theta > \pi/2$), a very common condition found in stalactites. This confirms the result obtained by Camporeale and Ridolfi [7], whereas the downstream migration for $\theta < \pi/2$ is instead a novel finding.

The effect of slope is now investigated by the ratios $r_\omega = \omega_{\mathrm{I},\max}(\theta)/\omega_{\mathrm{I},\max}(\pi/2)$, $r_\alpha = \alpha_{\max}(\theta)/\alpha_{\max}(\pi/2)$ and $r_{v_p} = v_{p,\max}(\theta)/v_{p,\max}(\pi/2)$, that quantify the extent of the alteration
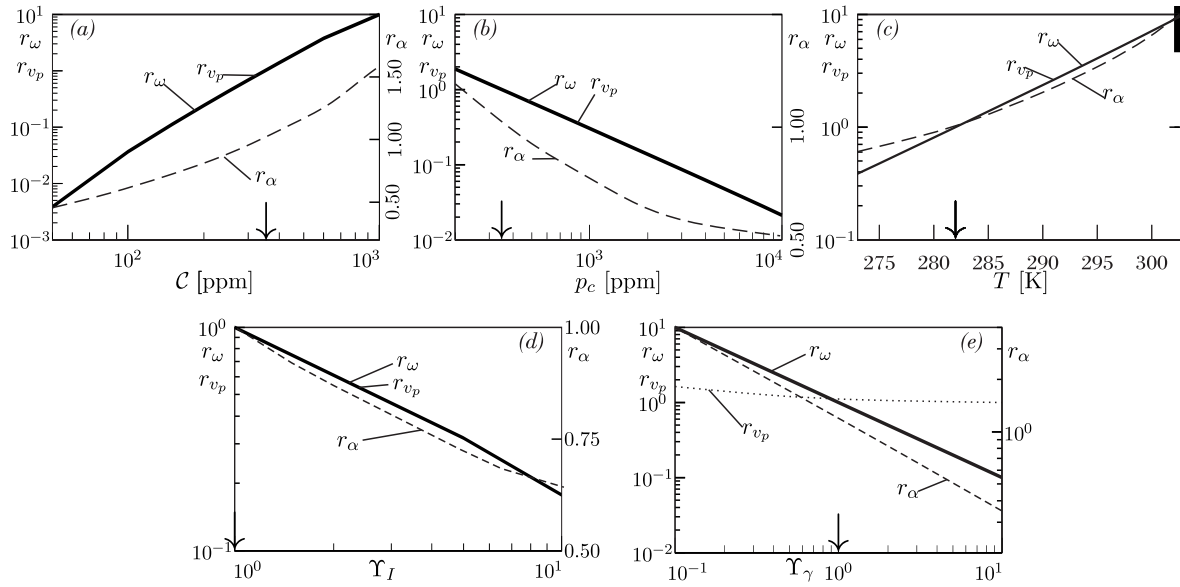
Figure 8. Dependence of r_ω, r_α and r_{v_p} on $\mathcal{C}$, p_c, T, Υ_I and Υ_γ. The vertical arrow marks the benchmark condition.

of the pattern characteristics (i.e., growth rate, most amplified wavenumber and phase velocity) if the wall slope is changed from $\theta = \pi/2$. Such ratios are evaluated for different Reynolds numbers and only for unstable conditions (i.e., $\omega_{I,max} > 0$).

It can be observed (figure 7c) that lowering the mean slope of the calcite wall induces a strong reduction of the growth rate, that eventually becomes negative. On the contrary, in overhanging slopes the growth rate is amplified of more than one order of magnitude. This feature is more pronounced for high Reynolds numbers. The wall slope plays a strong influence also in selecting the most unstable wavelength (see panel 7d): for low Reynolds numbers ($R < 10^{-3}$) the pattern wavelength increases up to five times by reducing the slope below $\pi/2$, while weaker changes are observed if θ is increased above $\pi/2$. Differently, for higher Reynolds numbers ($R > 10^{-2}$) the pattern wavelength is weakly influenced by a reduction of the slope below $\pi/2$, while it reduces up to one fourth by increasing θ above $\pi/2$.

Finally, the wall slope affects the crenulation phase velocity (panel 7e). We have previously demonstrated (see panel 7b) that the crossing of the wall slope threshold $\theta = \pi/2$ induces a switch in the direction of migration of crenulation. Panel 7f shows that high Reynolds numbers ($R \sim 10^{-1}$) induce a dramatic increment in the absolute value of the phase velocity.

(e) Impact of water chemistry on crenulation dynamics

The effect of water chemistry and temperature is here investigated systematically. To this aim, we follow the same approach used in the previous section by focusing on the ratios $r_\omega = \omega_{I,max}(l)/\omega_{I,max}(l_B)$, $r_\alpha = \alpha_{max}(l)/\alpha_{max}(l_B)$ and $r_{v_p} = v_{p,max}(l)/v_{p,max}(l_B)$ that quantify the extent of the alteration on the pattern characteristics if a control parameter is changed from the benchmark value, l_B, to the new value, l. The ratios are evaluated by changing the parameters of the benchmark set one by one. The analysis has been repeated for different Reynolds numbers, but no appreciable differences were observed, and all the curves evaluated for different R collapse on the same line.

Panel 8a shows that an increase of the concentration of calcium, $\mathcal{C}$, of the order of 10^2 leads to an increment of the maximum growth rate, $\omega_{I,max}$, up to three order of magnitudes. On the contrary, when carbon dioxide partial pressure p_c increases, the maximum growth rate $\omega_{I,max}$

reduces up to two order of magnitudes (panel 8*b*). From a physical point of view, the higher is the degree of over-saturation of the solution, the faster crenulations form and it can also be observed (line r_α) that the most amplified wavenumber undergoes significantly changes (the ratio r_α is in the range $[0.5, 1.6]$). It follows that the chemical composition of the incoming water has an appreciable effect in selecting the dominant wavelength. Finally, the phase velocity of the most unstable wavenumber has a behaviour very similar to the growth rate; in fact, $v_{p,\max}$ undergoes a strong increase when the calcium concentration $\mathcal{C}$ increases, while it decreases for high values of carbon dioxide partial pressure.

Let us examine now the role of thermal changes. The temperature modifies a number of physical and chemical parameters of the system (e.g., water density, viscosity, surface tension, equilibrium constants of the chemical reactions, solubility products, etc.), but the main effects are a change in the solubility of calcite (that decreases with temperature) and in the solubility of carbon dioxide (decreasing with the temperature, as film de-gassing is promoted). The final result is therefore an increment of the growth rate of the instability with temperature. From a quantitative point of view, variations of temperature of a few tens of degrees cause changes of the maximum growth rate and of the phase velocity up to two order of magnitudes, while the selection of the most amplified wavenumber is less influenced (r_α remains in the range $[0.9, 1.5]$, panel 8*c*). Such response of the system to changes of the water chemistry and temperature is not surprising. In the subsections (c), we have in fact demonstrated that the dilution mechanism is the ultimate responsible of the destabilization of the film-calcite interface. In section (b), we have also shown that the strength of dilution mechanism is proportional to $(\rho_1 + 2\rho_3)\mathcal{F}\hat{d}\mathcal{I}(0)/\chi$ (see Eq. 4.1). It follows that the higher the term $\mathcal{F}$, the higher the destabilizing strength of the dilution mechanism. The calcite precipitation rate, $\mathcal{F}$, that occurs in unperturbed conditions only depends on the calcium concentration $\mathcal{C}$, carbon dioxide partial pressure p_c and temperature T.

It is now instructive to investigate the role of the water chemistry activity in the crenulation dynamics. In particular, we consider the introduction of other chemical species in the $\mathrm{Ca}^{2+} - \mathrm{HCO_3}^- - \mathrm{H_2O}$ ternary solution. This is common in underground waters where other cations and anions can be found. We recall (see Sec. 2.b) that the introduction of new ions alters the solution total activity I. In particular, the addition of the chemical i induces in the solution activity an increment $z_i^2[X_i]/2$. It follows that small concentrations $[X_i]$ of ions that have high ionic charge (e.g., $z_i{=}3{-}7$) can significantly increase the solution activity and reduce the activity of the single different chemicals. In order to quantify the role of additional ions, we introduce a coefficient $\Upsilon_I \geq 1$ that multiplies the solution activity $I = 3[\mathrm{Ca}^{2+}]$ adopted in the previous analysis. In this way, we model an increment of the solution activity caused by the presence in the water of generic elements other than calcium- and bicarbonate-ions and water. It can be observed (see bold line in figure 8*d*) that an increment of solution activity (increasing Υ_I) has a moderate influence on the maximum growth rate $\omega_{\mathrm{I},\max}$ and on the phase velocity $v_{p,\max}$. The effects of an increase of the solution activity resemble those caused by the increase of the carbon dioxide partial pressure (figure 8*b*). Physically, the increment of the solution activity causes the reduction of the activity coefficients γ_i and, despite the concentrations $[X_i]$ are unaffected, the activity (X_i) of the chemicals involved in calcite deposition is reduced. In turn, the unperturbed calcite deposition rate $\mathcal{F}$ and the crenulation growth rate diminish (we already demonstrated that the growth rate is proportional to $\mathcal{F}$). Quantitatively speaking, variations of I cause changes of $\omega_{\mathrm{I},\max}$ and of $v_{p,\max}$ that are lower than one order of magnitude (panel 8*d*). Also the most amplified wavenumber (dashed line in figure 8*d*) results poorly affected by the solution activity, being r_α in the range $[0.75, 1]$.

Finally, the effect of the alteration of the liquid surface tension is explored. This point is not practically relevant, since a reduction of water surface tension is only possible through the action of a surfactant. Nevertheless, this analysis is theoretically instructive as it further clarifies the significance of the film flow dynamics on the crenulation development. To this aim, we introduce the coefficient $10^{-1} \leq \Upsilon_\gamma \leq 10^1$ that multiplies the surface tension γ (accordingly, the capillary length l_c is multiplied by $\Upsilon_\gamma^{1/2}$). It turns out that variations of the surface tension have noticeable
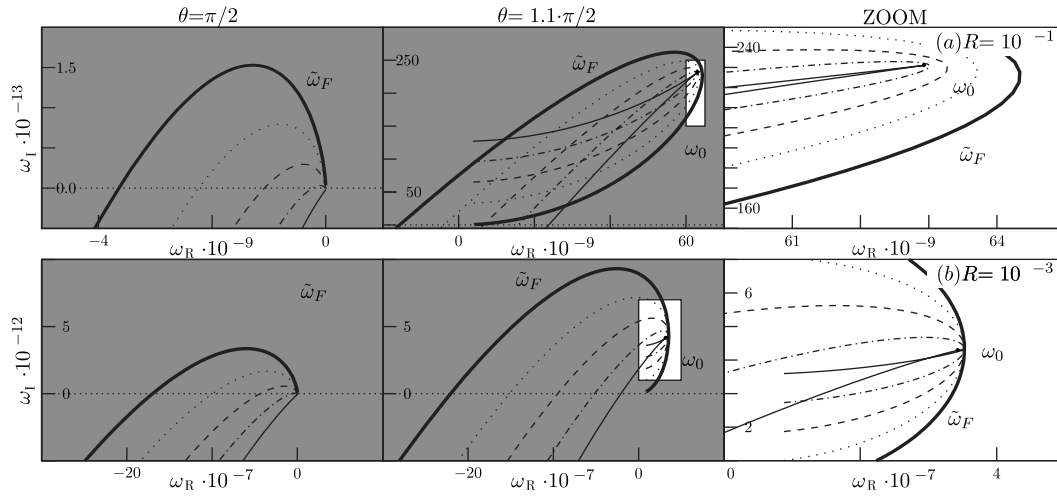
Figure 9. Cusp maps in the ω-plane for $\theta = \pi/2$ (left panels), $\theta = 1.1 \cdot \pi/2$ (central and right panels), and two different Reynolds numbers. The right panels are a zoom in of the white box reported in the central panels. Thick continuous lines describe $\tilde{\omega}_F$, the other lines refer to $\Omega(\alpha_I^*)$. The exact values of the adopted α_I^*, are reported in table 2. The coordinates in the ω−plane of the branch points are: $\omega_0 = 6.2 \cdot 10^{-8}$+2.3i$\cdot 10^{-11}$ (for $R = 10^{-1}$); and $\omega_0 = 3.5 \cdot 10^{-7}$+4.3i$\cdot 10^{-12}$ (for $R = 10^{-3}$). Other parameters are $\{T, p_c, \mathcal{C}\} = \{T_B, p_{c,B}, \mathcal{C}_B\}$.

Table 2. Values of I for different R and corresponding to different line style in figure 9. The first value refers to $\theta = 1.1 \cdot \pi/2$ while the second value within brackets refers to $\theta = \pi/2$

R	10^{-1}	10^{-3}
dotted	$-8 \cdot 10^{-5}(-2 \cdot 10^{-5})$	$-1 \cdot 10^{-6}(-1 \cdot 10^{-6})$
dashed	$-16 \cdot 10^{-5}(-4 \cdot 10^{-5})$	$-2 \cdot 10^{-6}(-2 \cdot 10^{-6})$
dot-dash	$-24 \cdot 10^{-5}(-6 \cdot 10^{-5})$	$-3 \cdot 10^{-6}(-3 \cdot 10^{-6})$
thin continuous	$-32 \cdot 10^{-5}(-8 \cdot 10^{-5})$	$-4 \cdot 10^{-6}(-4 \cdot 10^{-6})$

effects on the crenulation growth rate (bold line in figure 8e) as well as a relevant impact on the selection of the most amplified wavenumber (dashed line in figure 8e). This is a further proof that film flow dynamics, and in particular the free surface response to a bottom topography, plays a key role also in selecting both wavenumber of the pattern (a common feature in many free surface flow–induced morphologies [36]) and the pattern growth rate.

5. Convective/absolute nature of the crenulation instability

The assessment of the convective/absolute nature of an instability is a key information in unstable open flow hydrodynamic systems [34], as well as in morphodynamic problems [37,38]. A system is convectively unstable if the response to an impulsive perturbation increases in time but migrates and decays to zero at all the spatial locations, and it is absolutely unstable if the response grows exponentially in time at all spatial locations. Convectively unstable systems behave as "noise amplifiers", displaying extrinsic dynamics, since in the absence of continuous forcing the response decays back to zero, whereas absolutely unstable systems are characterized by intrinsic dynamics and behave as 'oscillators' [39,40]. From a practical point of view, the knowledge of the type of instability is fundamental for correctly understanding field observations and for an appropriate set up of numerical simulations and experiments.

In order to discriminate between these two kinds of instabilities, one needs to determine if the wave with the zero group velocity is growing (absolute case) or decaying (convective case). This is an easy task only in a limited number of cases, where the dispersion relation is provided analytically. Unfortunately, this is not the case for crenulations, which require a refined modelling of the flow field along the non-homogeneous vertical direction. In order to circumvent this difficulty, we will apply the so-called cusp map method [38,41] to the present problem.

By definition, the complex *absolute wavenumber* α_0 characterizes the long time behaviour of eq. (3.15) at x fixed, and it corresponds to the solution of the saddle point condition, $D(\omega, \alpha) = \omega_{,\alpha}(\alpha) = 0$, provided that the *causality principle* is satisfied, i.e. that α_0 is a pinch point. Moreover, $\omega_{0I} = \text{Im}[\omega(\alpha_0)]$ is the associated *absolute growth rate*. If only real wavenumbers are considered, equation $\omega_{I,\alpha} = 0$ is satisfied by the wavenumber $\alpha_{\max}$ which displays the maximum temporal growth rate $\omega_{I,\max} = \omega_I(\alpha_{\max})$. The instability is convective if $\omega_I(\alpha_{\max}) > 0$ and $\omega_{0I} < 0$; on the contrary, the flow is absolutely unstable if $\omega_I(\alpha_{\max}) > 0$ and $\omega_{0I} > 0$. Recalling that the $j-$th spatial branch of the dispersion relation $\alpha_j(\bar{\omega}_I)$ associated with the growth rate $\bar{\omega}_I$ is the locus of complex wave numbers in which $\omega_I(\alpha) = \bar{\omega}_I$, it can be demonstrated that points where $\omega_{,\alpha} = 0$ are pinch points only if at least two spatial branches $\alpha_m(\omega_{0I})$ and $\alpha_n(\omega_{0I})$ pinching in α_0 are well confined within opposite α_I half-planes when ω_I is increased [40].

The pinch point criterion usually requires a mapping from the complex frequency plane to the complex wave number plane, thus the dispersion relation has to be solved for α as a function of ω. Unfortunately, in many physically relevant cases (e.g., the water-calcite interface evolution herein investigated), the dispersion relation is a transcendental function of α while it is polynomial only in ω. In order to circumvent this difficulty, Kupfer [41] refined a work by Derfler [42] and developed a technique – called cusp map method – for the assessment of the convective/absolute nature of the instability requiring only a $\alpha \to \omega$ mapping.

The cusp map method basically follows two conceptual steps: (i) to detect the points that have null group velocity in the complex ω-plane, and (ii) to determine whether these zero group velocity complex frequencies are actually pinch points in the complex wavenumber plane or not. The former task is accomplished recalling that (in the frequency plane) a point ω_0 that satisfies $D(\omega_0, \alpha) = D_{,\alpha}(\omega_0, \alpha) = 0$ (the saddle point condition) and $D_{,\alpha\alpha}(\omega_0, \alpha) \neq 0$, has a local map $(\omega - \omega_0) \sim (\alpha - \alpha_0)^2$. From a topological point of view, this implies that when a curve lying in the complex α-plane and passing trough α_0 is mapped into the complex ω-plane, it displays a cusp-like singular point at the branch point ω_0. Kupfer [41] suggested to map the contour $\alpha_I = \alpha_I^*$, progressively lowering α_I^* from zero. The mapping of all the contour points with $\alpha_I = \alpha_I^*$ generates in the complex frequency plane the curve $\Omega(\alpha_I^*)$. A branch point is obtained when $\Omega(\alpha_I^*)$ displays a cusp-like singularity (occurring at ω_0), and this occurs exactly when $\alpha_I^* = \text{Im}(\alpha_0)$. Finally, the check for the pinch point condition is performed by considering the relative position of ω_0 with respect to $\tilde{\omega}_F$, the latter being the mapping of $\alpha_I^* = 0$ into the the ω-plane (i.e., the usual temporal branch). It can be demonstrated that branch points ω_0 that are "covered" an odd number of times by $\tilde{\omega}_F$ are pinch points [41].

The results obtained by the application of the cusp-map method to the crenulation instability are provided in figure 9 for different values of R and θ. The curve $\tilde{\omega}_F$ and some others curves $\Omega(\alpha_I^*)$ are reported in the ω-plane, with α_I^* progressively lowering from zero. Left panel refers to the case $\theta = \pi/2$ while the central panel refers to $(\theta = 1.1 \cdot \pi/2)$.

For $\theta = \pi/2$, lowering α_I^* from 0 causes a progressive lowering of the contours until the whole curve $\Omega(\alpha_I^*)$ lies in the half plane $\omega_I < 0$. Even thought α_I^* is progressively reduced, no singular points (clue of a zero-group-velocity wave) can be found. It follows that for $\theta = \pi/2$ there are no unstable waves (instability would require $\Omega(\alpha_I^*)$ to lie in the half plane $\omega_I > 0$) that exhibit null group velocity. Therefore, the calcite-flow interface is convectively unstable.

For $\theta = 1.1 \cdot \pi/2$, lowering α_I^* from zero causes a progressive sharpening of the contours $\Omega(\alpha_I^*)$ that ultimately leads to the occurrence of a singular point at ω_0. In order to show more clearly the selected cusp, an enlarged view of the zone where the cusp is forming (white box in the central part surrounding the branch point ω_0) is reported in the right part of each panel. Once the branch

Table 3. Effect of the increment of the parameter reported in the top row. "⇑ / ⇓" strong increment/decrement, "↑ / ↓" weak increment/decrement.

Parameter	R	$\mathcal{C}$	p_c	T	θ
Growth rate	⇓	⇑	⇓	⇑	↑ / ⇑
Wavelength	⇑	↓	↑	↓	⇓
Phase velocity	⇓	⇑	⇓	⇑	↓ / ⇓

point is detected, its position is compared with respect to $\tilde{\omega}_F$ and it turns out that ω_0 is "covered" only once by $\tilde{\omega}_F$. The branch points in the ω-plane therefore correspond to pinching points in the α-plane. It follows that, being $\omega_{0I} > 0$, the calcite-flow interface is absolutely unstable for any R here considered.

The dependence of the nature of the instability on θ has been thoroughly scrutinized, revealing that $\theta = \pi/2$ is a critical value for any value of the other control parameters: for $\theta > \pi/2$ crenulations are absolutely unstable while for for $\theta \leq \pi/2$ the instability is convective.

This is a key result. From the definition of convective instability and from the behaviour of other convectively unstable systems [43], it is in fact known that exists a critical length L_c of the domain below which the macroscopic detection of the instability is not possible. Moreover, the lower is the perturbation growth rate, the higher becomes this critical length L_c. We also recall that variations of the chemo-physical control parametrs (e.g. a wall slope reduction, see figure 7c) can cause dramatic reductions of the growth rate of crenulations. It follows that in some cases (e.g., wall slope below $\pi/2$, little over-saturation of the water), the critical length L_c is very large. In particular, L_c can exceed the speleothem size. As a consequence, the pattern of crenulations cannot be macroscopically detected. This justifies the difficulty of observing crenulations in some caves (little over-saturation of the water) or in some specific speleothems (wall slope below $\pi/2$).

Consider now the emblematic case of one stalactite (wall slope above $\pi/2$) hanging over its associated stalagmite ($\theta < \pi/2$): the total flow rates of the films dripping on both speleothems are equal. Moreover, stalagmites usually have a radius much larger than the associated stalactite. It follows that stalagmites, in principle, exhibit smaller values of Reynolds number than stalactites. These conditions lead the stalagmites to fall either in the stable region of figure 7a or, at most, in the convectively unstable regime but with a very low growth rate ($\theta < \pi/2$), both cases being unfavourable to pattern detection. However, provided a sufficient length, the pattern detection remains possible, as testified by the occurrence of regular dune-like patterns on long flowstones.

6. Discussion and concluding remarks

In this work we have presented the results of a detailed physical- and chemical-based mathematical model that predicts the formation of crenulations as the result of a morphological instability of the water film-calcite interface. We have firstly demonstrated that carbon dioxide transport can be neglected, and that only the concentration of calcium at the wall plays a relevant role in determining the stability of the system, namely the occurrence or not of crenulations. This aspect allows the development of future simplified modelling approaches that only focus on calcium transport, even though the complete set of geochemical reactions is fundamental for obtaining the basic state solutions. The possibility of disregarding the carbon dioxide transport allowed us to develop a simplified dispersion relation that shows the physiochemical processes involved in the crenulations instability. In particular, we have distinguished two main processes that affect the calcium concentration at the wall: the *depletion* and the *concentration* mechanisms. The former is related to the consumption of calcium ions near the wall, as a result of calcite deposition, and is showed to be stabilizing. The latter is instead destabilizing, and it is related to the alteration of the calcium concentration depth-profile induced by the free surface dynamics. Similar mechanism where also found in the analysis of the formation of ripples over icicles [2,44], where the heat flux is the key process driving the morphological evolution of the ice wall. We also

suspect that the ripple-like patterns that often shape silica sinters [45] are induced by the fluid free surface, but a rigorous analysis that explains how the film dynamics interact with the cooling processes responsible of the sinters formation [46] is still lacking.

We have then investigated the role of many physical (e.g., Reynolds number, average slope) and chemical (e.g., calcium ion concentration, carbon dioxide partial pressure and temperature) parameters involved in the crenulation dynamics, demonstrating that their variations in realistic ranges cause very significant changes in some key control features. A synthesis of the key results is reported in table 3, where the effect of the increment of a given parameter (top row) on the growth rate, phase velocity and most unstable wavenumber is reported. It is a key point to notice that the wavelength of the instability (that is easily measurable and stored in speleothems stratigraphy) is influenced especially by the Reynolds number and by the wall slope. Such strong dependence of the pattern wavelength on R and θ opens the possibility to associate a particular wavelength to past flow conditions that occurred at the time of the calcite deposition. Differently, many parameters affects the growth rate. In particular we observe high growth rate only for very over-saturated water. It should therefore not be surprising that in several caves where water over-saturation is weak, crenulations are not visible: the film-calcite interface is unstable, but the amplitude of the crenulation pattern grows so slowly that cannot be detected. Anyway, nonlinear analysis are required for gaining further insights about the temporal evolution of the crenulation amplitude.

The convective/absolute nature of the instability has finally been assessed: crenulations are invariably absolutely unstable for $\theta > \pi/2$ (typical wall slope in stalactites) while they are convectively unstable for $\theta \leq \pi/2$. The evaluation of the convective/absolute nature of the instability allows the assessment of the robustness of the results obtained from these paleo-hydraulic reconstructions. In particular, the use of convectively unstable crenulations' features requires some caution, because they can result from the amplification of some external disturbance rather than the mirror of an intrinsic dynamics that can be well associated to some flow or environmental characteristics [39]. Differently, the reconstructions of paleo–flows well fit with the case of absolutely unstable crenulations. Anyway, the actual use of crenulation wavelength for the interpretation and estimation of paleo–flows requires further experimental efforts to validate the theoretical outcomes here presented.

Data accessibility This manuscript does not contain primary data and as a result has no supporting material associated with the results presented.

Authors contributions All the authors equally contributed in developing the the mathematical model, performing the analysis, interpreting the results and writing the paper. All authors gave final approval for publication.

Conflict of interests The authors have no competing interest.

References

1   A. Fowler, *Mathematical geoscience*, 1st ed. (Springer, 2011).
2   C. Camporeale and L. Ridolfi, "Ice ripple formation at large Reynolds numbers," J. Fluid Mech. **694**, 225–251 (2012a).
3   K. Ueno, "Characteristics of the wavelength of ripples on icicles," Phys. Fluids **19** (2007).
4   P. Blondeaux, "Mechanics of coastal forms," Annu. Rev. Fluid Mech. **33**, 339–370 (2001).
5   G. Seminara, "Fluvial sedimentary patterns," Annu. Rev. Fluid Mech. **42**, 43–66 (2010).
6   M. B. Short, J. C. Baygents, J. W. Beck, D. A. Stone, R. S. Toomey, and R. E. Goldstein, "Stalactite growth as a free-boundary problem: A geometric law and its platonic ideal," Phys. Rev. Lett. **94**, 018501 (2005).
7   C. Camporeale and L. Ridolfi, "Hydrodynamic-driven stability analysis of morphological patterns on stalactites and implications for cave paleoflow reconstructions," Phys. Rev. Lett. **108**, 238501 (2012b).
8   M. Short, J. Baygents, and R. Goldstein, "Stalactite growth as a free-boundary problem," Phys. Fluids **17** (2005).

9   C. Hill and P. Forti, *Cave Minerals of the World* (National Speleological Society, 1997).

10 P. Meakin and B. Jamtveit, "Geological pattern formation by growth and dissolution in aqueous systems," Proc. R. Soc. Lond., A **466**, 659–694 (2010).

11 C. Hawkins, L. Angheluta, O. Hammer, and B. Jamtveit, "Precipitation dendrites in channel flow," EPL **102** (2013).

12 S. Nesic, "Key issues related to modelling of internal corrosion of oil and gas pipelines âĂŞ a review," Corros. Sci. **49**, 4308 – 4338 (2007).

13 F. McDermott, D. Mattey, and C. Hawkesworth, "Centennial-scale holocene climate variability revealed by a high-resolution speleothem delta O-18 record from SW Ireland," Science **294**, 1328–1331 (2001).

14 I. Fairchild, C. Smith, A. Baker, L. Fuller, C. Spotl, D. Mattey, F. McDermott, and EIMP, "Modification and preservation of environmental signals in speleothems," Earth-Sci. Rev. **75**, 105–153 (2006).

15 O. Nilsson and J. Sternbeck, "A mechanistic model for calcite crystal growth using surface speciation," Geochim. Cosmochim. Acta **63**, 217–225 (1999).

16 L. N. Plummer, T. M. L. Wigley, and D. L. Parkhurst, "Kinetics of calcite dissolution in Co2-water systems at 5-degrees-C to 60-degrees-C and 0.0 to 1.0 atm CO2," Am. J. Sci. **278**, 179–216 (1978).

17 M. Reddy, "Crystallization of calcium-carbonate in presence of trace concentrations of phosphorus-containing anions ," J. Cryst. Growth **41**, 287–295 (1977).

18 W. House, "Kinetics of crystallization of calcite from calcium bicarbonate solutions," J. Chem. Soc. Faraday Trans. **77**, 341–359 (1981).

19 W. Dreybrodt, *Processes in Karst systems: physics, chemistry, and geology* (Springer-Verlag, 1988).

20 W. Dreybrodt and D. Buhmann, "A mass-transfer model for dissolution and precipitation of calcite from solutions in turbulent motion," Chem. Geol. **90**, 107–122 (1991).

21 O. Hammer, D. K. Dysthe, B. Lelu, H. Lund, P. Meakin, and B. Jamtveit, "Calcite precipitation instability under laminar, open-channel flow," Geochim. Cosmochim. Acta **72**, 5009–5021 (2008).

22 R. Wooding, "Growth of natural dams by deposition from steady supersaturated shallow flow ," J. Geophys. Res. **96**, 667–682 (1991).

23 G. Kaufmann, "Stalagmite growth and palaeo-climate: the numerical perspective," Earth Planet. Sci. Lett. **214**, 251–266 (2003).

24 P. Y. Chan and N. Goldenfeld, "Steady states and linear stability analysis of precipitation pattern formation at geothermal hot springs," Phys. Rev. E **76**, 046104 (2007).

25 A. Wierschem, M. Scholle, and N. Aksel, "Vortices in film flow over strongly undulated bottom profiles at low Reynolds numbers," Phys. Fluids **15**, 426–435 (2003).

26 H.-C. Chang and E. Demekhin, *Complex wave dynamics on thin films* (Elsevier, 2002).

27 P. Kapitsa and S. Kapitsa, "Wave flow of thin liquid layers," Zh. Eksp. Teor. Fiz **19**, 105–120 (1949).

28 D. Buhmann and W. Dreybrodt, "The kinetics of calcite dissolution and precipitation in geologically relevant situations of karst areas .1. Open system," Chem. Geol. **48**, 189–211 (1985).

29 G. Kaufmann and W. Dreybrodt, "Calcite dissolution kinetics in the system CaCO3-H2O-CO2 at high undersaturation," Geochim. Cosmochim. Acta **71**, 1398–1410 (2007).

30 R. Robinson and R. Stokes, *Electrolyte Solutions* (Dover Publications, 2002).

31 M. M. Reddy, L. N. Plummer, and E. Busenberg, "Crystal-growth of calcite from calcium bicarbonate solutions at constant pCO2 and 25-degrees-C a test of a calcite dissolution model," Geochim. Cosmochim. Acta **45**, 1281–1289 (1981).

32 A. Pentecost, *Travertine* (Springer, 2005).

33 D. Gloss and H. Herwig, "Wall roughness effects in laminar flows: an often ignored though significant issue," Exp. Fluids **49**, 461–470 (2010).

34 P. Huerre and P. A. Monkevitz, "Local and global instabilities in spatially developing flows," Annu. Rev. Fluid Mech. **22**, 473–537 (1990).

35 B. Jones, R. Renaut, R. Owen, and H. Torfason, "Growth patterns and implications of complex dendrites in calcite travertines from Lysuholl, Sn ae fellsnes, Iceland," Sedimentology **52**, 1277–1301 (2005).

36 R. Vesipa, C. Camporeale, and L. Ridolfi, "A shallow-water theory of river bedforms in supercritical conditions," Phys. Fluids **24** (2012), 10.1063/1.4753943.

37 C. Camporeale and L. Ridolfi, "Convective nature of the planimetric instability in meandering river dynamics," Phys. Rev. E **73**, 026311 (2006).

38 R. Vesipa, C. Camporeale, L. Ridolfi, and J. Chomaz, "On the convective-absolute nature of river bedform instabilities," Phys. Fluids **26** (2014).

39 P. Huerre and M. Rossi, "Hydrodynamic instabilities in open flows," in *Hydrodynamic and instabilities*, edited by C. Goldreche and P. Manneville (Cambridge University Press,Cambridge, 2000) pp. 159–229.

40 A. Bers, "Space-time evolution of plasma instabilities – absolute and convective," in *Handbook of Plasma Physics*, edited by M. Rosenbluth and R. Sagdeev (North Holland,Amsterdam, 1983) pp. 159–229.

41 K. Kupfer, A. Bers, and A. K. Ram, "The cusp map in the complex-frequency plane for absolute instabilities," Phys. Fluids **30**, 3075–3082 (1987).

42 H. Derfler, "Frequency cusp, a menas for discriminating between convective and nonconvectibe instability," Phys. Rev. A **1**, 1467–1471 (1970).

43 C. Di Cristo, M. Iervolino, A. Vacca, and B. Zanuttigh, "Minimum channel length for roll-wave generation," J. Hydr. Res. **46**, 73–79 (2008).

44 K. Ueno, "Pattern formation in crystal growth under parabolic shear flow. II," Phys. Rev. E **69** (2004).

45 N. Herdianita, P. Browne, K. Rodgers, and K. Campbell, "Mineralogical and textural changes accompanying ageing of silica sinter," Miner. Depos. **35**, 48–62 (2000).

46 B. Mountain, L. Benning, and J. Boerema, "Experimental studies on New Zealand hot spring sinters: rates of growth and textural development," Can. J. Earth Sci. **40**, 1643–1667 (2003).

Supplementary Material of "Thin-film induced morphological instabilities over calcite surfaces"

Riccardo Vesipa[1], Carlo Camporeale[1], Luca Ridolfi[1]

[1]Department of Environmental, Land and Infrastructure Engineering,
Politecnico di Torino, Italy

1 Reaction constants of the chemical model

The reaction constants of the chemical model are listed in table 1.

Table 1: Equilibrium constants of the chemical model [1].

$\log K_W$	$[\text{mol}^2 \; \text{l}^{-2}]$	$22.801 - 4787.3T^{-1} - 0.010365T - 7.1321 \log T$
$\log K_H$	$[\text{mol} \; \text{l}^{-1} \; \text{atm}^{-1}]$	$108.3865 - 6919.53T^{-1} + 0.01985076T - 40.45154 \log T + 669365T^{-2}$
$\log K_C$	$[\text{mol} \; \text{l}^{-1} \; \text{atm}^{-1}]$	$-171.9065 - 0.077993T + 2839.319T^{-1} + 71.595 \log T$
$\log K_2$	$[\text{mol} \; \text{l}^{-1}]$	$-107.8871 + 5151.79T^{-1} - 0.03252849T + 38.92561 \log T - 563713.9T^{-2}$
$\log K_5$	$[\text{mol} \; \text{l}^{-1}]$	$1.707 \cdot 10^{-4}$
$\log \kappa_1$	$[\text{cm} \; \text{s}^{-1}]$	$0.198 - 444T^{-1}$
$\log \kappa_2$	$[\text{cm} \; \text{s}^{-1}]$	$2.84 - 2177T^{-1}$
$\log \kappa_3$	$[\text{mmol} \; \text{cm}^{-2} \; \text{s}^{-1}]$	$-5.86 - 317T^{-1}$ for $T < 298.15$
		$-1.10 - 1737T^{-1}$ for $298.15 < T < 321.15$
$\log \kappa_4$	$[\text{cm}^4 \; \text{mmol}^{-1} \; \text{s}^{-1}]$	$-2.375 + 0.025(T - 273.15)$ for $p_c > 0.05$atm
		$-2.375 + 0.025(T - 273.15) + 0.56(-\log p_c - 1.3)$ for $p_c < 0.05$atm
$\log k_1^+$	$[\text{s}^{-1}]$	$329.850 - 110.54 \log T - 17265.4T^{-1}$
$\log k_1^-$	$[\text{s}^{-1}]$	$13.558 - 3617.1T^{-1}$
$\log k_2^+$	$[\text{s}^{-1}]$	$13.635 - 2895T^{-1}$
$\log k_2^-$	$[\text{l} \; \text{mol}^{-1} \; \text{s}^{-1}]$	$14.09 - 5308T^{-1}$

2 Parameters of the Debye-Hückel theory

The parameters of the Debye-Hückel theory are listed in table 2.

Table 2: Coefficients for the Debye-Huckel equation [1].

Ion	$d_i \; [10^{-10} \; \text{m}]$	$e_i \; [\text{l} \; \text{mol}^{-1}]$	z_i
Ca^{2+}	5.0	0.165	+2
H^+	9.0	–	+1
HCO_3^-	5.4	–	-1
CO_3^{2-}	5.4	–	-2
OH^-	3.5	–	-1
$A = 0.4883 + 8.074 \cdot 10^{-4}(T - 273.15)$			
$B = 0.3241 \cdot 10^{10} + 1.600 \cdot 10^{-4}(T - 273.15)$			

3 Derivation of the simplified PWP equation

In order to obtain Eq. (2.9) from the complete PWP equation (2.8), the first step is to approximate the solution pH to a function of the incoming calcium concentration $\mathcal{C}$. To this aim, the definition of the solubility product

equilibrium constant of calcite, K_c, is re-arranged to $[CO_3^{2-}] = \mathcal{A}/[Ca^{2+}]$ where $\mathcal{A} = K_c/(\gamma_{Ca^{2+}}\gamma_{CO_3^{2-}})$, then $(2.4e)$ is written as $[CO_3^{2-}] = \mathcal{B}[HCO_3^-]/[H^+]$ with $\mathcal{B} = K_2\gamma_{HCO_3^-}/(\gamma_{H^+}\gamma_{CO_3^{2-}})$. By equalling these two expression of $[CO_3^{2-}]$, one can isolate the term $[HCO_3^-]$, obtaining the relation $[HCO_3^-] = \mathcal{A}[H^+]/\mathcal{B}[Ca^{2+}]$ that, substituted into the simplified form of the electroneutrality equation (2.7), gives $[H^+] = 2[Ca^{2+}]^2\mathcal{B}/\mathcal{A}$. We neglect the space dependence of pH and, therefore, relate $[H^+]$ with the initial depth-averaged calcium concentration $\mathcal{C}$ rather than with the local calcium concentration $[Ca^{2+}]$. We therefore obtain the relation between the solution pH and the incoming calcium concentration as $[H^+] = a_3\mathcal{C}^2$, where $a_3 = 2\mathcal{B}/\mathcal{A}$.

The following step is to relate the bicarbonate concentration to the calcium concentration. Being (see the previous paragraph) $[H^+] = a_3\mathcal{C}^2$, $[CO_3^{2-}] = \mathcal{B}[HCO_3^-]/[H^+]$, and (from Eq. $2.4a$) $[OH^-] = \mathcal{D}/[H^+]$, where $\mathcal{D} = K_W/\gamma_{OH^-}\gamma_{H^+}$, the full electroneutrality condition (2.6) can be recast as

$$[HCO_3^-]\left(1 - \frac{2\mathcal{B}}{a_3\mathcal{C}^2}\right) = 2[Ca^{2+}] + \frac{a_3^2\mathcal{C}^4 - \mathcal{D}}{a_3\mathcal{C}^2}. \tag{1}$$

From this last equation we evaluate the dimensionless concentration of bicarbonate, that reads $c_3 = a_1c_1 + a_2$, where $a_1 = 2(a_3\mathcal{C}^2)(a_3\mathcal{C}^3 - 2\mathcal{B}\mathcal{C})^{-1}$ and $a_2 = (a_3^2\mathcal{C}^4 - \mathcal{D})(a_3\mathcal{C}^3 - 2\mathcal{B}\mathcal{C})^{-1}$.

The last step is to use the approximated relations for $[H^+]$ and for $[HCO_3^-]$ obtained in the two previous paragraphs for simplifying the PWP equation. In particular, we substitute $[H^+]$ with $a_3\mathcal{C}^2$ and $[HCO_3^-]$ with $c_3 = (a_1c_1 + a_2)\mathcal{C}$. Moreover, we make use of the expression $[H_2CO_3^0] = \mathcal{E}[H^+][HCO_3^-]$ – obtained from $(2.4c)$, where $\mathcal{E} = \gamma_{H^+}\gamma_{HCO_3^-}/K_5$ – and of the scaling $\tilde{f} = (\tilde{u}_f/\varrho)f$. We finally obtain

$$f = \rho_0 + \rho_1 c_1 + \rho_2 c_2 + \rho_3 c_1^2, \tag{2}$$

where

$$\rho_0 = -a_3\mathcal{C}^2\frac{\varrho}{\tilde{u}_f}(\kappa_1\gamma_{H^+} + \mathcal{C}a_2\kappa_2\gamma_{H_2CO_3^0}\mathcal{E} + \frac{\kappa_3}{a_3\mathcal{C}^2}), \quad \rho_1 = \frac{\varrho}{\tilde{u}_f}(\mathcal{H}p_c\kappa_2), \tag{3a, b}$$

$$\rho_2 = \frac{\varrho}{\tilde{u}_f}(-\gamma_{H_2CO_3^0}\kappa_2\mathcal{E}a_3\mathcal{C}^3 a_1 + \kappa_4\gamma_{Ca^{2+}}\gamma_{HCO_3^-}\mathcal{C}^2 a_2), \quad \rho_3 = \frac{\varrho}{\tilde{u}_f}(\gamma_{Ca^{2+}}\gamma_{HCO_3^-}\kappa_4\mathcal{C}^2 a_1). \tag{4a, b}$$

Typical values of such coefficients are listed in table 3.

Table 3: Range of values of the dimensionless coefficients ρ_0 to ρ_3 evaluated for $T \in [277, 303]$ K, $\mathcal{C} \in [50, 1000]$ ppm, $p_c \in [10, 10000]$ ppm, $R \in [10^{-4}, 10^{-1}]$, and $\theta = \pi/2$.
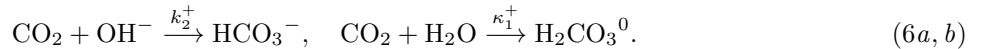
$\rho_0 \cdot 10^{-6}$	$\rho_1 \cdot 10^{-6}$	$\rho_2 \cdot 10^{-8}$	$\rho_3 \cdot 10^{-4}$
$8.8 - 1200$	$3.5 - 7400$	$1.9 - 5.8$	$2.6 - 2700$

4   Derivation of the net production of the carbon dioxide

Carbon dioxide is only involved in the two reactions $(2.4c, d)$, that can be summarized in the two production-reaction

$$HCO_3^- \xrightarrow{k_2^-} CO_2 + OH^-, \quad H^+ + HCO_3^- \xrightarrow{\kappa_a} CO_2 + H_2O, \tag{5a, b}$$
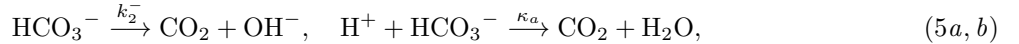
and in the two reactions of consumption

$$CO_2 + OH^- \xrightarrow{k_2^+} HCO_3^-, \quad CO_2 + H_2O \xrightarrow{\kappa_1^+} H_2CO_3^0. \tag{6a, b}$$

The net production of the carbon dioxide is therefore $\tilde{r}_2 = (k_2^- + k_a[H^+])[HCO_3^-] - (k_2^+[OH^-] + k_1^+)[CO_2]$. After scaling, we introduce the relations $[OH^-] = \mathcal{D}/[H^+]$, $[H^+] = a_3\mathcal{C}^2$, and $c_3 = a_1c_1 + a_2$, (whose derivation was shown in the section 3 of this Supplementary Material) finally obtaining

$$r_2 = -k_1 c_2 + k_2(a_1 c_1 + a_2), \quad k_1 = (k_1^+ + k_2^+\frac{\mathcal{D}}{a_3\mathcal{C}^2})\frac{\tilde{D}}{D_2}, \quad k_2 = (k_2^- + k_1^-\mathcal{E}a_3\mathcal{C}^2)\frac{\tilde{D}}{D_2\mathcal{H}p_c}. \tag{7a, b, c}$$

5 Theoretical justification of the quasi-steady approximation

The complete mathematical model has four temporal derivatives. In order to consider only those relevant for the considered morphological problem, the analysis of the timescale of the different dynamical processes involved is required. To this aim we introduce the scalings $\tilde{f} = \mathcal{C}\bar{f}$ and $\tilde{t} = (\tilde{D}/\tilde{u}_f \varrho \mathcal{C})\bar{t}$ instead of $\tilde{f} = f/\varrho$ and $\tilde{t} = (\tilde{D}/\tilde{u}_f)t$, where the hat denotes variables made dimensionless with the new scaling. In this way, in the dimensionless equations $(2.2a)$, $(2.3a)$, $(2.9b)$, and (2.11) the dimensionless calcite flux reads $\varrho \mathcal{C}\bar{f}$ instead of $\tilde{f}$ while the dimensionless time reads $\bar{t}/\varrho \mathcal{C}$ instead of $\tilde{t}$. It follows that $(2.9b)$ becomes $\eta_{,\bar{t}} = \bar{f}$ while all the $\bar{t}$-derivatives in $(2.2a)$, $(2.3a)$ and (2.11) are multiplied by the factor $\varrho \mathcal{C} = \mathcal{O}(10^{-3})$, thus they are not quantitatively relevant in the mathematical model and can be disregarded. From a physical point of view, this means that the morphological temporal evolution of the wall is much slower ($\sim 10^3$ times) than the temporal dynamics of the film. It follows that hydrodynamics can be considered adiabatically slaved to the bed topography evolution.

6 Evaluation of the term $\hat{d}$

In order to simplify the evaluation of the term $\hat{d}$, it is useful to reduce the number of variables. To this aim, the pressure perturbation $\hat{p}$ is eliminated through a standard trick: at the first-order, the linearised horizontal (x-) component of $(2.2a)$ is ζ-derived, and the vertical (ζ-) component is multiplied by $-i\alpha$ so that, in their sum, pressure disappears. The stream function $\psi(\zeta)$ is then introduced. It satisfies the continuity equation and allows the velocities perturbation to be written as $\hat{u} = \hat{\psi}' - \Gamma$ and $\hat{w} = -i\alpha\psi$, where $\Gamma = \mathcal{U}'(1 + \hat{d}\zeta)$. In this way, the Navier-Stokes equations $(2a)$ are recast in the form of the Orr-Sommerfeld equations

$$\left[(\mathrm{d}^2/\mathrm{d}\zeta^2 - \alpha^2)^2 - i\alpha R(2\zeta - \zeta^2)(\mathrm{d}^2/\mathrm{d}\zeta^2 - \alpha^2) - 2i\alpha R\right]\hat{\psi} = 0, \tag{8}$$

flanked by the boundary conditions

$$\hat{h} + \hat{\psi} = 0, \quad \hat{\psi}'' - \hat{h}(2 + \alpha^2) = 0, \quad \hat{\psi}''' - \hat{\psi}'(iR + 3\alpha)\alpha + i\alpha\hat{h}\left[\alpha^2 \mathrm{Ka}\left(\frac{2}{R^2 \sin\theta}\right)^{\frac{1}{3}} + 2\cot\theta\right] = 0, \quad (9a, b, c)$$

at $\zeta=1$, and

$$\hat{\psi} = 0, \quad \hat{\psi} + 2 = 0, \tag{9d, e}$$

at $\zeta=0$, being $\hat{h} = \hat{\eta} + \hat{d}$. A formal solution of the flow field, governed by (8) and (9), reads $\hat{\psi} = \iota_1\psi^{(1)} + \iota_2\psi^{(2)} + \iota_3\psi^{(3)} + \iota_4\psi^{(4)}$ where $\psi^{(j)}$ ($j = 1,...4$) are four particular independent solutions. According to the standard nomenclature [3], the equation (8) has an ordinary point ($\zeta_0 = 0$) at the liquid-solid interface and thus, by the Fuchs theorem, each particular solution $\psi^{(j)}$ can be expanded in Taylor series about ζ_0 as

$$\psi^{(j)} = \sum_{i=1}^{\infty} a_{j,i}\zeta^{i-1} \quad (j = 1,...4), \tag{10}$$

that has an infinite radius of convergence, due to the lack of singular points in the problem. By substituting (10) back in (8), and by grouping the coefficients by power of ζ, the recursive relation for the $i-$th term of (10) reads

$$a_{j,i} = \frac{i\alpha R}{I_1 I_3}\left[\frac{2k^2}{i\alpha R}I_3 a_{j,i-2} + 2I_4 a_{j,i-3} + \left(2 - \frac{k^4}{i\alpha R} - I_5\right)a_{j,i-4}k^2\left(a_{j,i-6} - 2a_{j,i-5}\right)\right], \tag{11}$$

where $I_p = (i - p)(i - p - 1)$. In order to introduce the boundary conditions at $\zeta = 0$, we first set $a_{1,1} = a_{1,2} = a_{2,1} = a_{2,2} = 0$, i.e., $\psi^{(1)}(0) = \psi^{(1)'}(0) = \psi^{(2)}(0) = \psi^{(2)'}(0) = 0$. In this way, it is easy to verify that $\iota_3 = 1$, $\iota_4 = 0$ and $a_{3,1} = 0$, $a_{3,2} = -2$. We further impose $a_{1,4} = a_{2,3} = 0$ and $a_{1,3} = a_{2,4} = 1$, while the term $a_{3,4}$ and all the other term with $i > 4$ can be evaluated form (11). The remaining unknowns (the two integration constants ι_1, ι_2 and the perturbation of the free surface $\hat{h}$) are obtained from the dynamic and kinematic conditions at the free surface, that can be recast in the linear algebraic problem

$$\begin{pmatrix} L_{10} & L_{20} & 1 \\ L_{12} & L_{22} & -(2 + \alpha^2) \\ \Gamma L_{11} - L_{13} & \Gamma L_{21} - L_{23} & \Omega \end{pmatrix}\begin{pmatrix} \iota_1 \\ \iota_2 \\ \hat{h} \end{pmatrix} = -\begin{pmatrix} L_{30} \\ L_{32} \\ \Gamma L_{31} - L_{33} \end{pmatrix}, \quad \Gamma = iR\alpha + 3\alpha^2. \tag{12}$$

$$L_{p0} = \psi^{(p)}(1) = \sum_{i=1}^{i=\infty} a_{p,i}, \quad L_{pq} = \frac{\mathrm{d}^q \psi^{(p)}}{\mathrm{d}\zeta^q}\bigg|_{\zeta=1} = \sum_{i=1}^{i=\infty}\left[\prod_{r=1}^{r=q}\right]a_{p,i}. \tag{13}$$

3

Previous analyses[2] have compared the analytical solution of the flow field with numerical solutions, finding an excellent agreement if at least hundred terms are kept in the series and if $R < 10^3$. This last condition is always satisfied in the problem here considered where $R < 10^{-1}$.

7   Evaluation of the terms $\mathcal{I}(0)$, $\mathcal{L}(0)$ and $\mathcal{M}(0)$

The same recursive approach used in the previous section for the evaluation of the term $\hat{d}$ is also adopted for obtaining the analytical solutions of $\mathcal{I}(\zeta)$, $\mathcal{L}(\zeta)$ and $\mathcal{M}(\zeta)$ appearing in equations (3.8) and (3.12). We firstly write these functions in term of the general solutions $\mathcal{I} = \iota_5 \mathcal{I}^{(1)} + \iota_6 \mathcal{I}^{(2)}$, $\mathcal{L} = \iota_7 \mathcal{L}^{(1)} + \iota_8 \mathcal{L}^{(2)}$ and $\mathcal{M} = \iota_9 \mathcal{M}^{(1)} + \iota_{10} \mathcal{M}^{(2)}$. Each general solution is then expanded in Taylor series about ζ_0 as

$$\mathcal{I}^{(j)} = \sum_{i=1}^{\infty} b_{j,i} \zeta^{i-1}, \ \mathcal{L}^{(j)} = \sum_{i=1}^{\infty} c_{j,i} \zeta^{i-1}, \ \mathcal{M}^{(j)} = \sum_{i=1}^{\infty} d_{j,i} \zeta^{i-1}, \qquad (14a, b, c)$$

with $j = 1, 2$. By substituting (14) back in (3.8a, 3.11a, 3.12a) and by grouping the coefficients by power of ζ, the recursive relations for the $i-$th term of (14) read

$$b_{j,i} = \frac{-1}{I_0 I_1} \left[iP_1 \alpha (2b_{j,i-3} - b_{j,i-4}) + \alpha^2 b_{j,i-2} \right], \qquad (15a)$$

$$c_{j,i} = \frac{-1}{I_0 I_1} \left[iP_2 \alpha (2c_{j,i-3} - c_{j,i-4}) + (\alpha^2 - k_1) c_{j,i-2} - \frac{a_1 k_2 \mathcal{F}}{\chi} (\iota_5 b_{1,i-2} - b_{2,i-2}) - A_i \right], \qquad (15b)$$

$$d_{j,i} = \frac{-1}{I_0 I_1} \left[iP_2 \alpha (2d_{j,i-3} - d_{j,i-4}) + (\alpha^2 - k_1) d_{j,i-2} - \frac{a_1 k_2}{\chi} (\iota_5 b_{1,i-2} - b_{2,i-2}) \right], \qquad (15c)$$

where, in (15b), A_i are the coefficient of ζ^{i-1} terms appearing in $\hat{r}_{\mathcal{L}}$ (see Eq. 3.10), whereas $A_i=0$ for $i > 4$. The boundary condition at $\zeta = 0$ (3.8b) is implemented by setting $b_{1,1} = b_{2,2} = 1$ and $b_{1,2} = b_{2,1} = 0$. In this way $\mathcal{I}^{(1)'}(0) = 0$ and (3.8b) is satisfied if $\iota_6 = -1$. All the other terms with $i > 2$ can be evaluated form (15a). The integration constant ι_5 is obtained from (3.8c), and reads $\iota_5 = \mathcal{I}^{(1)'}(1)/\mathcal{I}^{(2)'}(1) = \sum_{i=1}^{i=\infty} b_{2,i} / \sum_{i=1}^{i=\infty} b_{1,i}$. Similarly, the boundary conditions at $\zeta = 0$ (3.11b, 3.12b) are implemented by setting $c_{1,1} = c_{2,2} = d_{1,2} = -\iota_8 = 1$ and $c_{1,2} = c_{2,1} = \iota_{10} = 0$. In this way, $\mathcal{L}^{(1)'}(0) = \mathcal{M}^{(2)'}(0) = 0$ and (3.11b, 3.12b) are satisfied if $\iota_9 = 1/\hat{f}$. All the other terms with $i > 2$ can be evaluated form (15b, c). The integration constant ι_7 is obtained from (3.11c, 3.12c), and reads $\iota_7 = \sum_{i=1}^{i=\infty} c_{2,i} - d_{1,i} / \sum_{i=1}^{i=\infty} c_{1,i}$.

References

[1] G. Kaufmann and W. Dreybrodt, "Calcite dissolution kinetics in the system CaCO3-H2O-CO2 at high undersaturation," Geochim. Cosmochim. Acta **71**, 1398–1410 (2007).

[2] C. Camporeale and L. Ridolfi, "Ice ripple formation at large Reynolds numbers," J. Fluid Mech. **694**, 225–251 (2012).

[3] C. Bender and S. Orszag, *Advanced Mathematical Methods for Scientists and Engineers I: Asymptotic Methods and Perturbation Theory* (Springer, 1978).